atmosphere

MDPI

Article

Integrated Assessment and Technological Framework for High-Altitude Wind Energy

Xiong Song [1], Huawei Xiang [1], Lanqiang Gong [1], Wenyue Xue [2], Zijun Luo [2], Menglong Wang [2], Chunling Zhou [2], Hong Zhang [2], Zhe Cai [2] and Qiang Liu [2,*]

[1] Power China Guiyang Engineering Corporation Limited, Guiyang 550081, China; songxiong_gyy@powerchina.cn (X.S.); xianghw_gyy@powerchina.cn (H.X.); gonglq_gyy@powerchina.cn (L.G.)
[2] Nanjing Climblue Technology Co., Nanjing 211135, China; xuewenyue@climblue.com (W.X.); luozijun@climblue.com (Z.L.); wangmenglong@climblue.com (M.W.); zhouchunling@climblue.com (C.Z.); zhanghong@climblue.com (H.Z.); erin@climblue.com (Z.C.)
* Correspondence: markliu@climblue.com

Abstract

High-altitude wind energy offers a vast and comparatively stable renewable resource, yet its development in China lacks systematic assessment that integrates generation system characteristics. This study establishes a multi-scale evaluation framework for China's 1000 m altitude wind resources by coupling 45 years of ERA5 (ECMWF Reanalysis v5) data for 1980–2024, four nested WRF (Weather Research and Forecasting) simulations at 27, 9, 3 and 1 km for 2000–2024, and a standardized airborne wind energy power curve. The framework proceeds from reanalysis-based coarse screening, through WRF-based refinement, to a site-specific assessment, and it quantifies the effective wind speed, the wind power density and the annual equivalent full-load hours on a common basis. The results reveal pronounced regional and altitude-dependent distribution patterns. Core resource-rich zones, including the northern Qinghai–Tibet Plateau, central-eastern Inner Mongolia, and northeastern coastal areas, exhibit annual equivalent full-load hours exceeding 3000 h, with specific regions surpassing 4000 h, and 7.33% of mainland China exceeds the 4000 h screening threshold while 32.96% exceeds 3000 h. A two-stage siting procedure, combining reanalysis-based coarse screening with meteorological-model refinement, identifies 19 candidate grid cells in Inner Mongolia, Qinghai, Tibet and Northeast China and ranks them by resource quality. Detailed assessment of a representative coastal site in Jilin Province validates the framework's reliability, and it reproduces the observed wind speed, temperature and relative humidity at 1000 m above ground level, characterizing the prevailing southwesterly–westerly regime, its seasonal cycle and its diurnal variability. The generation-potential values reported here are idealized, resource-based estimates rather than predictions for a specific device. This study addresses critical gaps in China's high-altitude wind resource quantification, providing scientific foundations and technical guidance for strategic planning, engineering feasibility studies, and commercial deployment of high-altitude wind power systems.

Keywords: high-altitude wind energy; wind resource assessment; WRF model; wind farm site selection

Academic Editor: Massimiliano Burlando

Received: 29 July 2026
Revised: 11 October 2026
Accepted: 13 October 2026
Published: 29 October 2026

Copyright: © 2026 by the authors. Licensee MDPI, Basel, Switzerland. This article is an open access article distributed under the terms and conditions of the Creative Commons Attribution (CC BY) license.

1. Introduction

The global energy system is accelerating its transition towards low-carbon and sustainable development to address the dual challenges of climate change and energy security [1,2]. Wind energy, one of the most technologically mature and cost-competitive renewable energy sources, has been deployed on a large scale worldwide. By the end of 2025, the global cumulative wind power capacity exceeded 1299 gigawatts, with China firmly holding the top position worldwide with over 640 gigawatts of installed capacity [3–5]. However, current wind power development remains highly concentrated in near-ground spaces typically below 200 m, facing bottlenecks such as uneven resource distribution, strong intermittency of output, and increasingly saturated prime sites [6,7]. In China, the "Three North" regions possess abundant wind resources yet are geographically distant from the load centers in the central and eastern regions, resulting in severe "curtailment" issues. This underscores the urgency of exploring novel and stable renewable energy sources [8].

With increasing altitude, surface friction diminishes, leading to a significant increase in wind speed and a reduction in the turbulence. Consequently, wind energy at altitudes exceeding 500 m above ground level is regarded as a highly promising next-generation form of wind power utilization owing to its vast reserves, extensive distribution, and high stability [9,10]. Wind energy is proportional to the cube of wind speed. At altitudes of one kilometer above ground level, wind power density can be 5–50 times greater than that near the surface [11]. To harness this resource, airborne wind energy systems have emerged, with primary technical approaches divided into ground-based power generation (using the tension from tethered aircraft to drive ground generators) and airborne power generation (mounting wind turbines directly onto tethered aerial platforms, with electricity transmitted to the ground via the tether cable) [12–14]. Among these, tethered-aircraft-based aerial power generation systems offer a viable technical pathway for deploying high-power generators owing to their stability and substantial payload capacity.

Internationally, the research and development of high-altitude wind energy commenced in the 1970s, with nations such as the United States, Italy, and the Netherlands leading early conceptual design and prototype testing efforts [15,16], accumulating extensive experience in system design, materials, and control strategies. By contrast, high-altitude wind energy research in China commenced relatively late. Although it has received national policy attention during the 14th Five-Year Plan period, current R&D remains predominantly focused on foundational areas such as materials and components. Systematic engineering practice and commercialization exploration are still in a catch-up phase [17–19]. Currently, the core prerequisite constraining the large-scale application of this technology is the lack of refined, reliable, and power system-integrated assessments of the high-altitude wind energy potential at the national scale [20].

Existing research on China's wind energy resources predominantly relies on sounding data or global reanalysis materials with limited spatiotemporal resolution, struggling to capture localized wind flow characteristics in complex topographies. Even fewer studies have coupled wind resource data with the power characteristic curves of specific airborne power generation systems to quantify their actual electricity generation potential [21]. Consequently, although the high-altitude wind energy abundance of regions such as the Tibetan Plateau and Inner Mongolia Plateau is widely acknowledged, understanding their total resource volume, spatiotemporal distribution patterns, and specific sites suitable for industrial-scale development remains relatively vague.

To address these research gaps, this study aims to systematically assess upper-air wind resources across multiple altitude layers throughout China. It innovatively integrates long-term ERA5 reanalysis data, mesoscale WRF numerical simulations, and a power generation potential model based on typical airborne power generation system

https://doi.org/10.3390/atmos17111065

curves. This approach seeks to achieve the following core objectives: (1) to reveal the macro-scale distribution patterns and spatiotemporal variation in wind speed and power density across China's 500 m to 5000 m altitude range; (2) to introduce cut-in, rated, and cut-out wind speed thresholds for quantitative assessment of annual equivalent full-load operating hours and theoretical power generation potential across different regions; (3) to enhance assessment accuracy by obtaining high-resolution wind field data for key areas through WRF model dynamic downscaling; and (4) to establish a site-selection methodology that combines the resource endowment with qualitative engineering screening constraints, identifying and prioritizing candidate demonstration sites.

The findings of this study are expected to provide a crucial scientific rationale and data support for the strategic deployment of high-altitude wind energy technology in China, siting of demonstration projects, and future industrial development.

The development prospects of high-altitude wind energy in China are substantial. Because the wind speed increases and its short-term variability generally decrease with height within the troposphere, airborne and tethered systems can access a stronger and more persistent resource than conventional tower-mounted turbines. They also remove the need for a tower and foundation, reduce the land footprint, can be relocated between sites, and can track the seasonal migration of the high-wind band by adjusting their operating height. The resource quantified in this study therefore provides a direct motivation for developing a systematic assessment framework of the kind proposed here.

Systematic assessment of this resource nevertheless involves four categories of difficulty, and the framework adopted here is organized around them. The first is the resolution of the source data: global analyses such as ERA5 offer a homogeneous record long enough for climatological screening, but their grid spacing is coarser than the scales on which the wind field varies in mountainous terrain, so that they cannot by themselves support site-level decisions. The second is representativeness in complex terrain, where adjacent slopes and valley or gorge systems carry markedly different wind speeds and no single station can characterize the domain. The third is the characterization of the generation system, since the power curve, the cut-in, rated and cut-out speeds, the response of an airborne platform to non-stationary wind, and the losses of tether and generator all shape the attainable output, while no commercial high-altitude device yet provides a validated curve. The fourth is the incorporation of engineering feasibility into the ranking of candidate sites, because resource quality alone is a necessary but not a sufficient criterion: terrain slope, grid access, transport and construction cost can reorder otherwise comparable sites. In this study the first two difficulties are addressed by a two-tier strategy that combines 45 years of ERA5 data for coarse screening with nested WRF simulations down to 1 km for refinement, and the third by applying a single standardized power curve so that the national comparison remains internally consistent. The fourth is treated qualitatively through the screening constraints of Section 2.6, and its quantitative treatment, together with the sensitivity of the results to the choice of power curve, remains an open task. The solutions adopted here, and the challenges that remain, are identified as such in Sections 4.2 and 4.3.

The remainder of this paper is organized as follows. Section 2 describes the data and the multi-scale evaluation framework. Section 3 presents the national distribution of high-altitude wind resources and the detailed assessment of the candidate site. Section 4 discusses the physical mechanisms and the sources of uncertainty. Section 5 summarizes the main conclusions and the limitations of the approach.

2. Materials and Methods

2.1. Data Source

The core data foundation for this study was the ERA5 (fifth generation ECMWF atmospheric reanalysis of the global climate) global reanalysis meteorological dataset released by the European Center for Medium-Range Weather Forecasts. Through an advanced data assimilation system, ERA5 integrates observational data from multiple global sources (such as satellites, radiosondes, aircraft reports, and ground stations) with numerical model background fields, providing a globally consistent atmospheric state dataset with high spatiotemporal coherence [22–24]. This study employed 45 years of monthly ERA5 data spanning 1980 to 2024, featuring a spatial resolution of 0.25° × 0.25° and vertically divided into 137 pressure levels. The meteorological variables included the zonal wind component U, meridional wind component V, vertical wind component W, temperature T, relative humidity RH, pressure P, and geopotential Z (https://cds.climate.copernicus.eu/) (accessed on 20 July 2025). This dataset serves two primary purposes: first, to conduct macro-distribution and long-term trend analyses of China's upper-air wind energy resources; second, to provide initial fields and boundary conditions for mesoscale numerical models, enabling higher-resolution dynamic downscaling simulations.

For model simulation validation and assessment, sounding observations were retrieved from the University of Wyoming upper-air sounding archive (https://weather.uwyo.edu/upperair/sounding.shtml) (accessed on 20 July 2025). Three stations in contrasting climatic and topographic regions were used. Yanji, in Jilin Province (42.9° N, 129.5° E, ID 54292, 176 m), is the regular radiosonde station closest to the candidate site. Nagqu, in the interior of the Qinghai–Tibet Plateau (31.5° N, 92.1° E, ID 55299, 4508 m), and Xilinhot, on the Inner Mongolia Plateau (43.9° N, 116.1° E, ID 54102, 1013 m), lie outside the nested 1 km domain and are therefore compared against the 27 km outer domain that produces the national screening fields. For all three stations the complete set of hourly observations recorded during 2024 was collected, so that the validation rests on the same period and on the same temporal sampling at every station.

2.2. Data Preprocessing

As the ERA5 raw data describe height-level distributions using atmospheric pressure, it is difficult to correlate them directly with wind turbine parameters. Therefore, the target vertical stratification pattern must be determined based on wind resource assessment requirements, using ground height as the stratification criterion. Given that high-altitude wind energy remains in its developmental phase, with the current focus prioritizing lower elevations, stratification below 3000 m is relatively denser. This study employs the following target height layers for interpolation: 500 m, 1000 m, 1500 m, 2000 m, 2500 m, 3000 m, 4000 m and 5000 m. The conversion between geopotential and height above ground, and the interpolation methods applied to the pressure-level data, are described below.

The altitude above ground level (AGL) (in meters) for a given grid cell is

$$\mathrm{AGL} = \frac{\mathrm{Z} - \mathrm{Z_surface}}{\mathrm{g}} \quad (1)$$

where Z denotes the geopotential provided by ERA5 (unit: m^2/s^2), Z_surface represents the surface geopotential (unit: m^2/s^2), and g is the gravitational acceleration, approximately 9.8 m/s^2. The height above ground level is obtained by dividing the difference between the two geopotential fields by g [22].

Linear interpolation was employed to interpolate the wind speed components, temperature, humidity, and pressure elements from the reanalysis data, which were stratified by pressure, to the AGL layer. Relative humidity was interpolated using a logarithmic method, following standard wind energy practice [23].

Linear interpolation method.

$$y = \frac{y_1 - y_0}{x_1 - x_0}(x - x_0) + y_0 \quad (2)$$

Logarithmic interpolation method.

$$y = \frac{y_1 - y_0}{\ln P_1 - \ln P_0}(\ln P - \ln P_0) + y_0 \quad (3)$$

where x denotes the height above ground of the target layer; x_1 and x_0 represent the heights above ground of the nearest upper and lower atmospheric pressure layers relative to the target layer; y denotes the interpolated result of a certain parameter for the target layer; y_1 and y_0 denote the corresponding parameter values for the nearest upper and lower atmospheric pressure layers relative to the target layer.

2.3. WRF Model

To overcome the spatial resolution limitations of the ERA5 reanalysis data in complex terrain regions, this study employed the advanced Weather Research and Forecasting model (WRF4.2) for dynamic downscaling simulations, thereby obtaining more refined three-dimensional wind field information. The WRF model is a mature mesoscale numerical weather prediction system that is widely applied in meteorological research and high-resolution wind energy resource assessments [25]. The model was configured with four nested domains using a 3:1 nesting ratio. The outermost domain (D01) covered the entire territory of China and its neighboring regions at a horizontal resolution of 27 km; the second domain (D02) covered the primary resource-rich areas at 9 km; the third domain (D03) covered the key pre-selected grids at 3 km; and the innermost domain (D04) was centered on the candidate site (42.08° N, 128.02° E) at 1 km (Figure 1). Initial and lateral boundary conditions were derived from the ERA5 reanalysis at 0.25° resolution, updated every 6 h. The integration time step was 60 s for the outermost domain. The 25-year integration was carried out in monthly analysis periods: each period was initialized at 00:00 UTC on the first day of the month from the ERA5 reanalysis (a cold start, with no model state carried over between consecutive periods), and the first 6 h of each period (00:00–06:00 UTC) were discarded as spin-up. The hourly outputs of all periods were then concatenated into a continuous hourly record for 2000–2024, so that the archived simulation is fully defined by the namelist settings and the ERA5 boundary files. No nudging or data assimilation was applied. Land-surface processes were represented by the Noah scheme, using WRF default land-use and topography data. Hourly output was retained at the eight target height levels above ground over the whole simulation period.

The model comprised 35 vertical levels with the model top at 50 hPa, of which 14 levels were placed within the lowest 2 km. The grid dimensions, the integration time step, the spin-up period, the nesting strategy and the treatment of land use and topography are summarized in Table 1, together with the physical parameterization schemes.

Table 1. Configuration of the WRF simulation and of the physical parameterization schemes.

Configuration	Setting
Microphysics	Purdue Lin scheme [26]
Cumulus convection	Kain–Fritsch (new Eta) scheme [27–29]
Longwave radiation	RRTM scheme [30]
Shortwave radiation	Goddard shortwave [31]
Surface layer	Monin–Obukhov similarity scheme [32]

Land surface	Noah Land Surface Model [33]
Planetary boundary layer	Yonsei University (YSU) scheme [34]
Initial and lateral boundary conditions	ERA5 reanalysis, 0.25°, updated every 6 h
Nesting strategy	One-way, grid-spacing ratio 1:3
Integration time step	60 s (outermost domain)
Simulation period	2000–2024
Spin-up	6 h (00:00–06:00 UTC)
Restart procedure	Cold start from ERA5 at the beginning of each monthly segment; no restart file carried over
Grid dimensions (west–east × south–north)	D01: 151 × 121; D02: 301 × 301; D03: 301 × 301; D04: 201 × 201 grid points
Nudging/data assimilation	None
Land use and topography	WRF default static fields

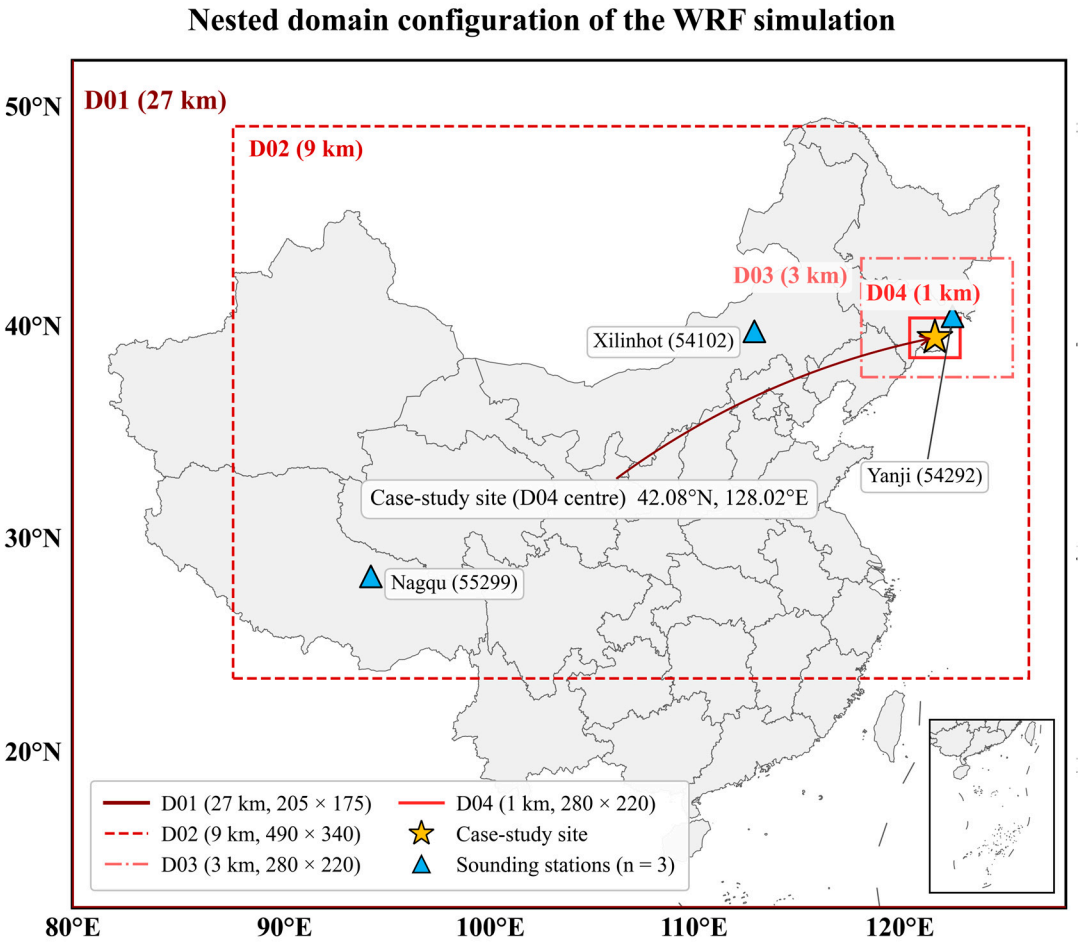


Figure 1. Domain setting of WRF model.

2.4. Evaluation of the Model Results

In the model evaluation section, the simulated meteorological elements (wind speed, relative humidity, and temperature) of the WRF model were validated against the actual data from radiosonde stations. The evaluation metrics included the correlation coefficient (R), the mean bias, defined as the average of the simulated minus the observed values, the root mean square error (RMSE) [35], and normalized mean bias (NMB) [36]:

$$R = \frac{\sum_{i=1}^{N}(Sim_i - \overline{Sim})(Obs_i - \overline{Obs})}{\sqrt{\sum_{i=1}^{N}(Sim_i - \overline{Sim})^2}\sqrt{\sum_{i=1}^{N}(Obs_i - \overline{Obs})^2}} \quad (4)$$

$$RMSE = \sqrt{\frac{\sum_{i=1}^{N}(Sim_i - Obs_i)^2}{N}} \quad (5)$$

$$NMB = \frac{\sum_{i=1}^{N}(Sim_i - Obs_i)}{\sum_{i=1}^{N} Obs_i} \quad (6)$$

where N is the number of samples; Sim_i and Obs_i are the simulated and the observed values at i time, respectively; and $\bar{S}im$ and $\bar{O}bs$ are the averages of the simulation and monitoring results at i time.

2.5. Wind Energy and Generation Potential Assessment Metrics

2.5.1. Key Wind Energy Parameters

Wind power density is the core physical quantity that characterizes the potential of wind energy. It is defined as the kinetic energy of the air passing through a unit area perpendicular to the flow per unit time and is calculated as

$$P = \frac{1}{2} \cdot \rho \cdot v^3 \quad (7)$$

where P denotes wind power density (unit: W/m^2), ρ represents air density (unit: kg/m^3), v denotes wind speed (unit: m/s), where ρ is computed from thermodynamic relations and gas constants [36–40]:

$$\rho = \frac{p_d}{R_d \cdot T} + \frac{rh \cdot e_s}{R_v \cdot T} \quad (8)$$

p_d denotes the dry air partial pressure (unit: Pa), R_d represents the dry air gas constant, 287.058 J/(kg·K), R_v denotes the water vapor gas constant, 461.5 J/(kg·K), rh and T denote relative humidity and air temperature, respectively, obtained directly from reanalysis data; e_s denotes the saturated water vapor pressure (unit: Pa) [36], computed with the Bolton (1980) formulation [38], which depends only on temperature. Over the temperature and humidity ranges encountered at the altitude levels considered here, this formulation differs from the enhanced formulation of Buck [39] by at most 0.8% in es, which propagates into a difference of less than 0.005% in air density and therefore has no material effect on the reported wind power densities:

$$e_s = 611.2 \cdot e^{\frac{17.67 \cdot (T - 273.15)}{T - 29.65}} \quad (9)$$

where e denotes the natural exponent, approximately equal to 2.718, and T represents the temperature (unit: K). Because the reference power curve is defined at standard air density, no correction for the reduction in air density with height (approximately 10% at 1000 m) was applied to the rated wind speed; this assumption is listed among the limitations in Section 4.2. The wind shear index α characterizes the shape of the wind speed profile curve as a power law exponent. This index quantifies the rate of wind speed variation

with height, with higher values indicating a greater increase in the wind speed height; the power-law description adopted here follows standard wind energy practice [36].

$$\alpha = \frac{\lg(V_2/V_1)}{\lg(Z_2/Z_1)} \quad (10)$$

where Z_1 and Z_2 denote the heights of the adjacent layers above and below the target height (unit: m); V_1 and V_2 represents the wind speeds corresponding to heights Z_1 and Z_2 (unit: m/s).

2.5.2. Power Generation Potential Assessment

Wind energy parameters reflect the inherent strength of wind energy at a specific location, rather than the actual power output of wind turbines. Assessing high-altitude wind energy resources requires further integration of engineering factors, such as turbine power curves, calculating annual equivalent full-load operating hours for a comprehensive evaluation. The reference generation system is defined by its power curve rather than by a specific commercial rating; the parameters adopted here are representative of demonstration-scale airborne wind energy concepts, and a single standardized curve was used so that the national comparison remains internally consistent. The key parameters are a cut-in wind speed of 4 m/s, a rated wind speed of 15 m/s and a cut-out wind speed of 30 m/s. The system generates rated power only at the rated wind speed, and the output is lower than the rated power at wind speeds above or below this value. Therefore, when calculating annual electricity generation, the relationship between wind speed and power must be considered:

$$\text{Annual Electricity Generation} = \sum_{i=0}^{n} a_i \quad (11)$$

where n represents the total number of hours in a year when the wind speed exceeds the cut-in speed but remains below the cut-out speed, a_i denotes the electricity generation corresponding to the hourly wind speed.

$$\text{Annual Generation Hour} = \frac{\text{Annual Electricity Generation}}{\text{Rated Power}} \quad (12)$$

A high annual generation hour count indicates stable wind resources, enabling the equipment to operate and generate electricity for most of the time and thus achieving a high utilization efficiency of the wind energy resource. The annual equivalent full-load operating hours are defined as the annual energy production divided by the rated power of the reference system; they are not the number of hours during which the wind speed exceeds the rated wind speed, and the theoretical capacity factor follows directly as the equivalent full-load hours divided by 8760 h. All generation-potential quantities reported in this study are idealized, resource-based estimates obtained by applying a standardized power curve to the simulated wind field. They characterize the wind resource rather than predicting the output of a specific airborne wind energy system, and they exclude the dynamic response of the airborne platform, tether and generator losses, and control-strategy efficiency.

2.6. Multi-Scale Siting Procedure

Based on the aforementioned assessment results, this study established a multi-scale collaborative site selection process combining "preliminary screening using reanalysis data with detailed calculations via meteorological models" to identify regions with the greatest development potential (in Figure 2). First, average wind speed fields at 500 m, 1000 m, 1500 m, 2000 m, 2500 m, 3000 m, 4000 m, and 5000 m were calculated using 45 years of data from 1980 to 2024, generating spatial distribution heatmaps of national wind speeds and wind power densities. Target height layers were selected considering the technical constraints and wind power generation benefits. Based on hourly WRF simulation

data for 2000–2024, the annual electricity generation totals and effective generation hours were calculated to assess the macro-level distribution characteristics of the high-altitude wind resource potential. Subsequently, candidate grid cells were identified by combining the resource-based ranking with readily available engineering constraints, namely the terrain slope, the distance to the nearest transmission line and substation, the distance to the nearest road, and the land-cover type. The terrain slope was computed from the 30 m Shuttle Radar Topography Mission (SRTM) digital elevation model; the locations of transmission lines, substations and roads were taken from the OpenStreetMap network (2024 extract); and the land-cover type was taken from the GlobeLand30 product. Grid cells with a mean slope above 15°, lying more than 50 km from the nearest transmission line or substation, more than 20 km from the nearest road, or classified as forest, water body, built-up or protected land were excluded before the resource-based ranking was applied. The outcome of this step should therefore be understood as a resource-based screening and prioritization, and a detailed engineering and economic feasibility assessment remains a task for subsequent site-specific studies. Detailed parameter assessments were conducted for the candidate sites. Wind rose diagrams were used to determine the prevailing wind directions, evaluate temporal variations in wind speed and power density, calculate wind shear indices, and statistically analyze wind frequency characteristics and seasonal variations. The overall framework within which this procedure is embedded is summarized in Figure 2b; of the five stages shown there, only the resource characterization and the refined site-specific analysis have been implemented in the present work, whereas the observational network, the multi-source integration and the operational service platform are identified as future work.

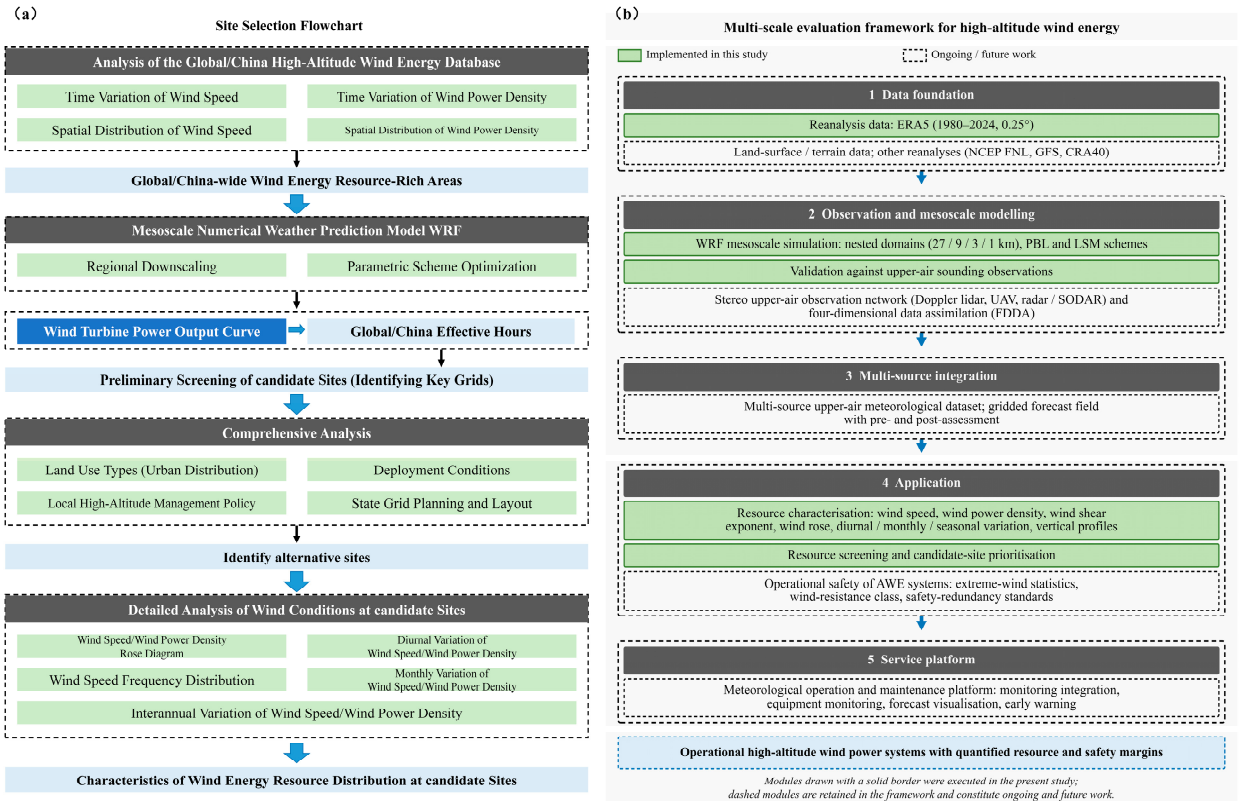


Figure 2. Multi-scale framework of the study: (**a**) the two-tier site-selection flowchart; (**b**) the multi-scale evaluation framework. In (**a**), blue arrows indicate the sequence of the procedure, dark gray bars denote the main stages, and blue bars denote the outputs of key steps; in (**b**), modules with solid borders were implemented in this study, while modules with dashed borders denote ongoing or future work.

3. Results

3.1. Macro-Level Distribution of Upper-Air Wind Energy Resources in China

Based on the distribution characteristics of average wind speeds from 1980 to 2024 (as shown in Figure 3), at the 500 m altitude level, the strong wind belt along the southeastern edge of the Qinghai–Tibet Plateau, influenced by the plateau-circumventing flow and the southern branch trough, forms the region with the highest national wind speeds of 20–30 m/s. A stable westerly jet stream extends from the Inner Mongolia Plateau to the Northeast Plain, sustaining wind speeds of 15–20 m/s and forming a continuous high-value belt. Wind speeds increase significantly with altitude along the southeast coast of China. At the 2000 m level, coastal regions, including Fujian, Zhejiang, and Guangdong, constitute another high-value zone, with speeds reaching 10–20 m/s. The Sichuan and Tarim Basins exhibit low wind speed zones (below 4 m/s) owing to topographical blocking. At the 5000 m altitude level, under the dominance of the westerly jet stream, national wind speeds generally rise above 15 m/s. Within the core region of the jet stream over the Qinghai–Tibet Plateau, wind speeds exceed 30 m/s, representing a 50% increase compared to the eastern plains at the same latitude.

Overall, China's wind energy resources exhibit distinct regional and altitude dependencies. Land areas generally show the highest wind speeds in the northwest (Qinghai–Tibet Plateau) and northeast (Inner Mongolia Plateau to Northeast Plains), followed by the southwest (Yunnan-Guizhou Plateau) and southeast coastal regions. Wind speeds near inland basins are relatively low, which is consistent with other studies [40]. Within China's maritime areas, wind speeds are notably higher in the Taiwan Straits. Wind speed exhibited an overall increasing trend with altitude.

Wind power density further amplifies the spatial variations in wind speed (as illustrated in Figure 4). China's core zones of high wind power density are predominantly concentrated within the westerly belt, with spatial distribution disparities intensifying progressively with increasing altitude. Specifically: below 1000 m, the Qinghai–Tibet Plateau, Yunnan-Guizhou Plateau regions, and areas of Inner Mongolia and Jilin in Northeast China exhibit the highest wind power densities, whereas the Taiwan Strait region within the maritime areas demonstrates the highest average wind power density. Above 3000 m elevation, influenced by the westerlies, China's northeastern coastal and southwestern regions exhibit the highest average wind speeds at upper altitudes. However, the frequent passage of typhoons in these areas increases the probability of equipment failure, necessitating further simulation of annual electricity generation totals to assess the economic viability of constructing wind power facilities in these areas. Southwestern plateau regions, such as Guizhou and Tibet, leverage the lifting effect of the westerlies and high-altitude topography to form zones of enhanced power density between 3000 m and 5000 m, presenting significant potential for wind energy resource development.

China's highest average wind power densities between 1980 and 2024 are predominantly concentrated in the Qinghai–Tibet Plateau, Yunnan-Guizhou Plateau, Inner Mongolia, Jilin, and other northeastern regions, as well as coastal areas such as Fujian and Zhejiang.

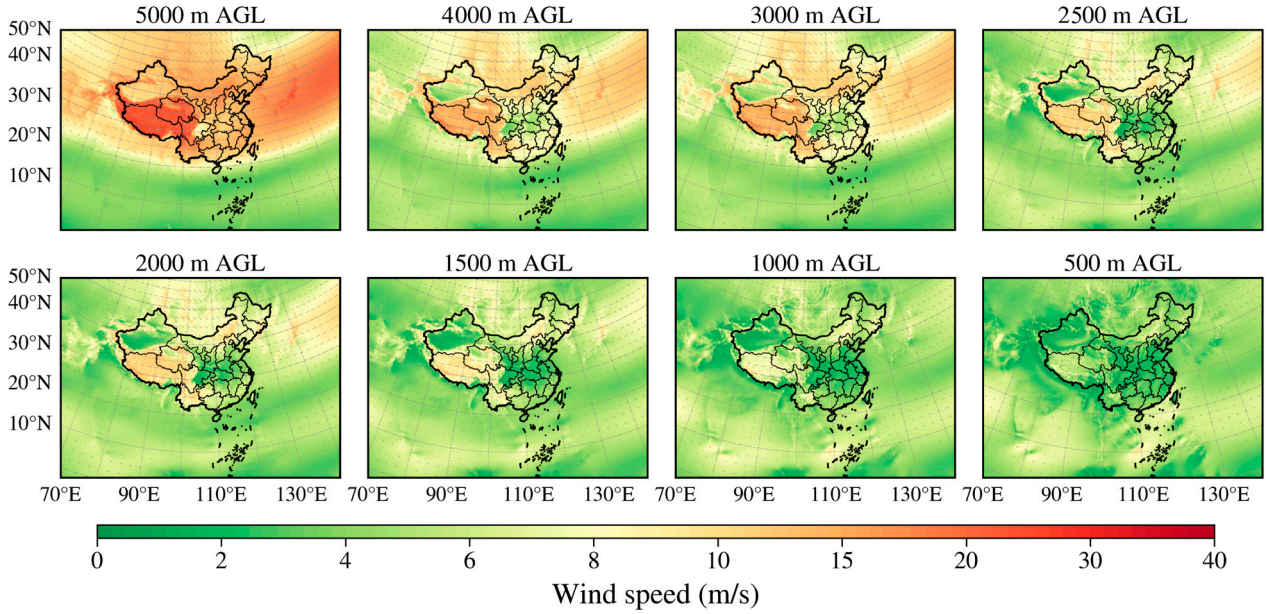


Figure 3. Wind field distribution at different altitudes in China, 1980–2024.

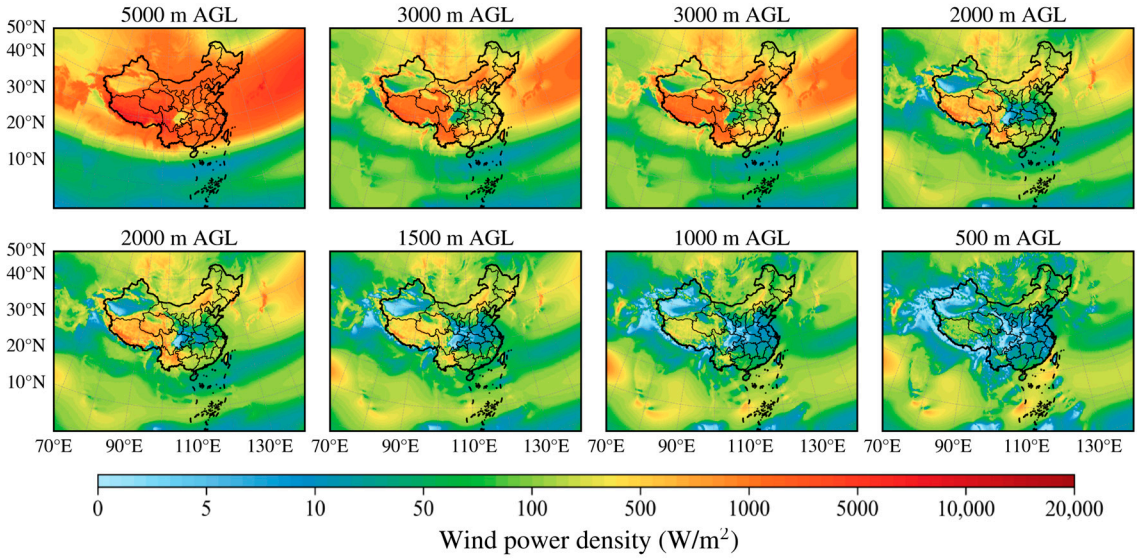


Figure 4. Distribution of wind power density at different altitudes in China, 1980–2024.

Based on ERA5 reanalysis data, an analysis of the interannual variations in wind speed and wind power density across different altitude layers in China from 1980 to 2024 (Figure 5a,b) revealed the following: Wind speeds at altitudes between 500 m and 1500 m exhibit high stability, with wind power density differences below 200 W/m². Resource increments are gradual, providing a reliable foundation for near-surface and upper-level wind power development. Wind speeds at 2000–3000 m exhibit a slight fluctuating upward trend, and the 4000–5000 m mid-to-upper tropospheric layer formed a wind speed extremum zone, with the 5000 m elevation establishing a persistent high-wind-speed core belt. Maximum wind speeds reach 17.2 m/s, and power density peaks at 1800–3000 W/m², though exhibiting pronounced interannual oscillations. This indicates uncertainties in mid-to-upper tropospheric boundary dynamics and high engineering implementation challenges.



Figure 5. Interannual variations at different altitudes in China, 1980–2024: (**a**) wind speed; (**b**) wind power density.

Monthly wind speed and power density across China (1980–2024), shown in Figure 6, exhibit strong seasonality driven by the East Asian Monsoon. Values peak in winter and reach a summer minimum, when the subtropical high suppresses turbulence, reducing power density to less than 20% of winter levels. Both variables increase with height (500–5000 m), with greater winter variability and the steepest gradient at 5000 m. The December–July wind speed difference widens from about 2 m/s at 500 m to 15 m/s at 5000 m, corresponding to a tenfold variation in power density.

China's wind energy exhibits a fundamental pattern characterized by "stronger in winter, weaker in summer; stronger at high altitudes, and more stable at lower levels". While the explosive growth of wind energy at 1500 m and above during winter holds development potential, the technical challenges posed by extreme fluctuations must be considered. Wind energy at 1000 m demonstrates greater stability, rendering resource development more feasible.

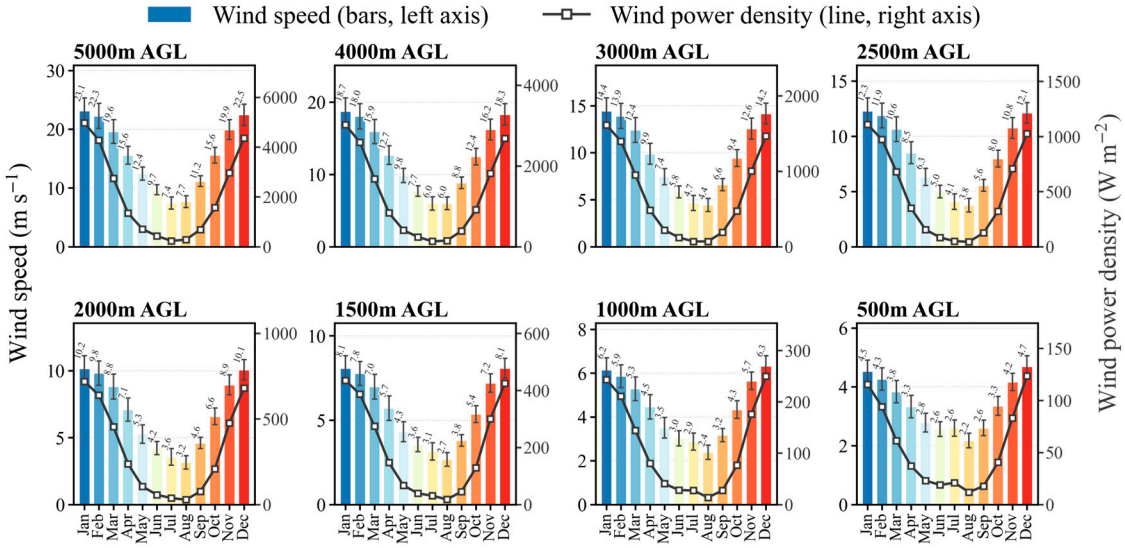


Figure 6. Monthly variations in wind speed (bars, left axis) and wind power density (line, right axis) at different altitudes across China, 1980–2024.

In summary, the wind power density in China exhibits pronounced regional and altitude dependencies. Considering the current conditions for high-altitude wind energy development, the 1000 m elevation offers abundant stable wind resources. This effectively avoids the extreme risks associated with installing wind turbines at 2000 m and above, while also providing valuable engineering experience for overcoming the technical challenges of developing higher-altitude wind resources. Therefore, in this study we choose 1000 m as a selected reference altitude for the assessment of high-altitude wind power, considering the balance across resource stability, technological maturity and economic viability. It remains a subject for future work about a demonstrated optimum.

3.2. Effective Wind Resources and Generation Potential

This section analyzes the effective wind speed, wind energy density, and annual generation hours based on nearly 25 years of meteorological data simulated by WRF from 2000 to 2024, combined with wind turbine power density curves.

Using a cut-in wind speed of 4 m/s and a cut-out wind speed of 30 m/s, combined with air density calculations, the spatial distribution of effective wind speeds at the 1000-metre altitude layer was derived (as shown in Figure 7a). High-value zones of effective wind speed (exceeding 10 m/s) are predominantly concentrated in the central-northern Qinghai–Tibet Plateau, western Inner Mongolia, and the coastal regions of Northeast China. These areas exhibit spatial distribution characteristics that are highly coupled with the pathways of the westerly jet stream and topographical forcing. Regions such as the Sichuan Basin, Tarim Basin, and middle-lower Yangtze River plains exhibit relatively low effective wind speeds owing to topographical shielding or stable atmospheric boundary layer stratification, presenting more limited resource development conditions. The effective wind speeds in China generally follow a west-high, east-low pattern, with plateau regions demonstrating superior conditions compared to plains.

Further calculations of wind power density (Figure 7b) revealed that high-value zones (exceeding 500 W/m^2) exhibit contiguous distribution patterns, concentrated in the central-northern Qinghai–Tibet Plateau, central Inner Mongolia, and the coastal regions of Northeast China. Within the plateau's interior, most areas surpassed 1000 W/m^2, demonstrating exceptional development potential.

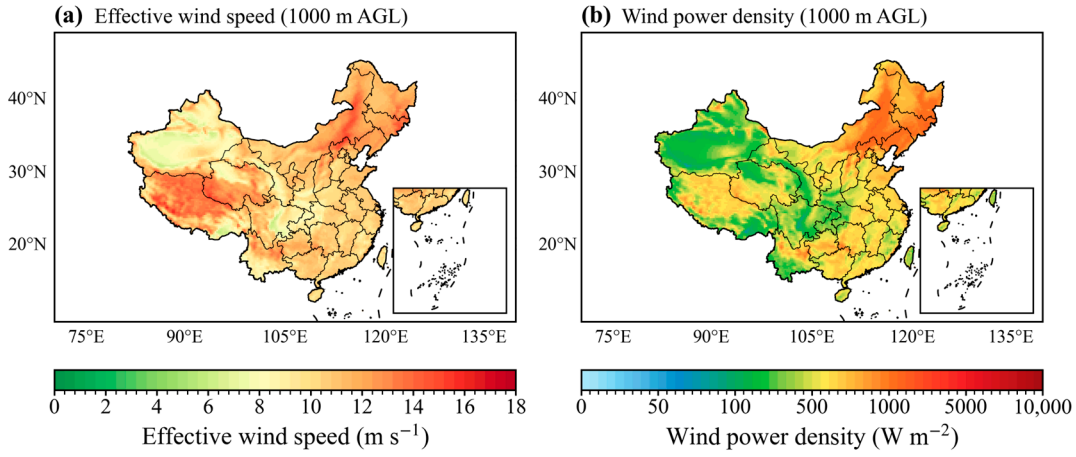


Figure 7. Spatial distribution in China, 2000–2024: (**a**) effective wind speed at 1000 m AGL; (**b**) wind power density at 1000 m AGL.

Preliminary estimates of the annual average generation hours were derived using the power curve of a 25 kW reference wind turbine with a rated wind speed of 15 m/s, as illustrated in Figure 8a. This 25 kW unit was chosen on engineering grounds as a demonstration-scale system for an airborne wind power feasibility study; it fits within the volume and payload envelope of the tethered aerostat, and its moderate rating keeps the initial capital investment and engineering validation requirements manageable. A single standardized power curve (cut-in 4 m/s, rated wind speed 15 m/s, cut-out 30 m/s) was therefore applied to all estimates to ensure internal consistency. The spatial distribution of annual average generation hours (Figure 8b) closely aligns with wind power density, further confirming the strategic importance of the Qinghai–Tibet Plateau, Inner Mongolia Plateau, and northeastern coastal regions as China's primary wind energy resource areas. The vast majority of these regions exceed 3500 h annual generation hours, with the Greater Khingan Range consistently achieving ultra-high levels of 4000 h or more. The data indicate that wind turbines in these areas could theoretically achieve capacity factors exceeding 45%. Stable secondary high-value areas, such as Northwestern Xinjiang and the southeastern coast, exhibit annual generation hours of 2000–3000, substantially outperforming low-altitude wind resources in most of eastern China and underscoring their strong development prospects.

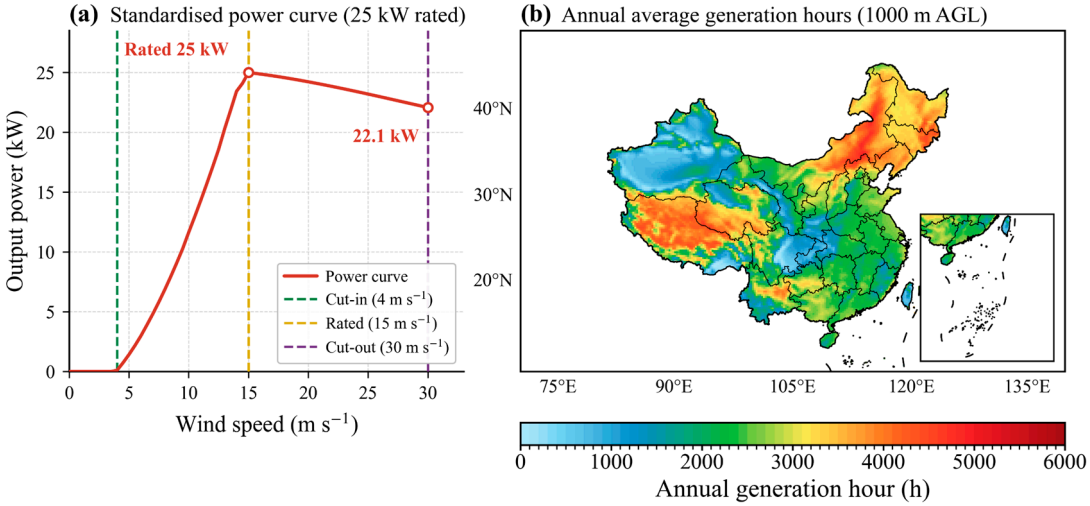


Figure 8. (**a**) Standardized power curve of the reference turbine; (**b**) annual average generation hours at 1000 m AGL in China, 2000–2024.

The primary quantitative criterion in this screening is the annual generation hours; economic viability is considered only qualitatively through the engineering constraints of Section 2.6. Analysis of China's 2000–2024 gridded (27 km) generation hour data shows that areas exceeding 4000 h (Figure 9b) cover approximately 7.33% of mainland China. In contrast, areas exceeding 3000 h (Figure 9a) account for 32.96%, extending the developable region into a contiguous zone covering the Northeast and eastern Inner Mongolia, as well as expanding viable areas in Qinghai and Tibet. Therefore, the 4000-h threshold is established as the preliminary screening criterion.

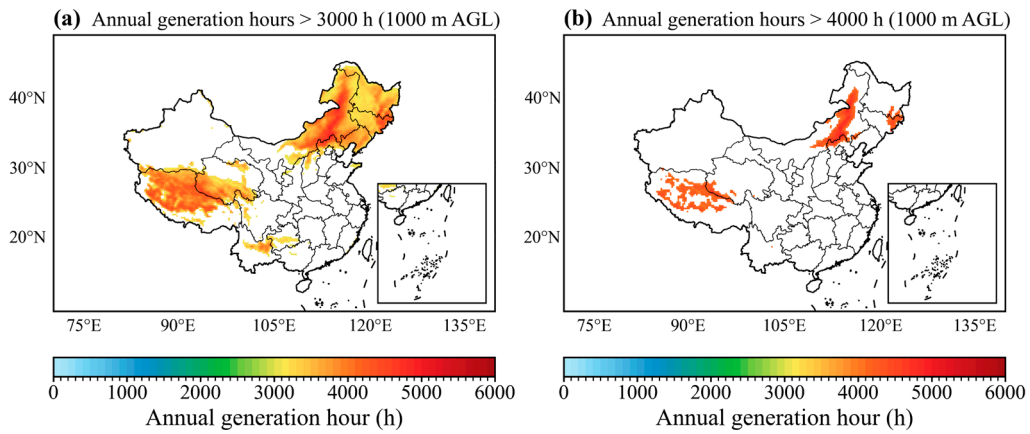


Figure 9. Projected annual generation hours in China, 2000–2024: (**a**) areas exceeding 3000 h; (**b**) areas exceeding 4000 h at 1000 m AGL.

Based on factors including generation hour levels, geographical concentration, and regional representativeness, qualified grid cells were categorized and assigned site selection priorities. The specific candidate sites are listed in Table 2. The first-tier sites, with annual generation hours exceeding 4700 h (specifically 4868–4970 h), exhibit outstanding resource endowments and are accorded priority for development. All five sites are exclusively concentrated in Inner Mongolia (117.24–120.14° E, 42.41–47.11° N), ranking 1st to 5th nationally. This cluster is well suited for large-scale wind farm deployment in resource terms; its grid-integration and construction conditions still require confirmation in site-specific studies.

The second-tier sites, ranging from 4550 to 4700 h, represent high-quality resources with considerable development potential. These five sites are predominantly located in Qinghai (three sites, ranks 47th, 81st, and 88th), with the remaining two in Northeast China (ranks 95th and 97th). Although the Qinghai sites are slightly inferior to those in Inner Mongolia, they remain highly attractive; the northeastern patches can serve as supplementary regional options and should be prioritized where grid access is feasible.

The third-tier sites, with annual generation hours between 4400 and 4550 h (specifically 4446–4544 h), offer moderate resources, somewhat lower than the preceding categories. These ten sites are scattered across Qinghai (three sites), Northeast China (four sites), and Tibet (three sites), and may be considered for supplementary or localized development.

Table 2. Classification and site selection priorities of candidate grid cells.

Level	Annual Generation Hours (h)	Longitude	Latitude	Region	National Ranking
First-tier grid	4969.61	117.31	42.66	Inner Mongolia	1
	4897.13	117.25	42.41	Inner Mongolia	2
	4886.44	117.24	43.69	Inner Mongolia	3
	4872.57	120.14	47.11	Inner Mongolia	4
	4868.48	117.65	42.61	Inner Mongolia	5
	4674.04	91.17	33.27	Qinghai	47

Second-tier grid	4599.13	90.88	33.24	Qinghai	81
	4583.24	91.14	33.51	Qinghai	88
	4565.50	128.02	42.08	Northeast China	95
	4561.60	128.39	44.38	Northeast China	97
Third-tier grid	4544.45	90.84	33.48	Qinghai	106
	4524.85	128.27	44.14	Northeast China	115
	4504.41	92.09	33.12	Qinghai	123
	4496.00	92.12	32.87	Tibet	127
	4482.98	85.08	30.16	Tibet	133
	4465.18	129.02	43.42	Northeast China	140
	4461.97	93.23	31.01	Tibet	144
	4459.55	128.91	43.18	Northeast China	147
	4446.68	93.52	31.03	Tibet	154

In summary, the five first-tier sites are all located in Inner Mongolia and occupy the top five national rankings, offering the highest resource quality across the country. The second-tier sites are concentrated mainly in Qinghai, with a small number in Northeast China, while the third-tier sites are scattered across Qinghai, Northeast China, Tibet, and Yunnan. However, resource quality alone does not determine development priority. Inner Mongolia, despite its superior wind resource endowments, faces considerable logistical constraints due to its remote location and limited transportation infrastructure, which could substantially raise the capital costs of turbine delivery and project construction. In contrast, the northeastern sites, though slightly lower in generation hours, benefit from better grid accessibility and more developed transport networks, which makes them appear more favorable for near-term deployment on the basis of the engineering constraints considered in this screening. The comparison is qualitative: only the resource-based ranking is quantitative, and a full economic assessment is left to site-specific studies.

3.3. Detailed Assessment of Candidate Sites

To further validate the applicability of the high-altitude wind energy resource assessment methodology and refined simulation process, independent validation zones exhibiting both representative wind resources and distinctive geographical characteristics must be selected. Following a comprehensive comparison, a representative sampling grid measuring 1 km by 1 km, centered at 42.08° N, 128.02° E, was selected. A detailed analysis employed hourly meteorological data simulated for the period 2000–2024. Without considering the power characteristic curves of wind turbines, this grid exhibits the highest wind energy density at a 1000 m height level nationwide. Its topography and meteorological conditions are comparable to those of the candidate site grid described earlier. This facilitates a systematic demonstration of the technical analysis workflow, progressing from a macro-level resource assessment based on reanalysis data to a site-specific evaluation grounded in numerical simulation. This further provides a foundation for refined analyses, such as wind shear and turbulence intensity, based on ground-based monitoring equipment.

Table 3 and Figure 10 evaluate the simulation against sounding observations at 1000 m above ground level at three stations, all of which lie outside the 1 km nested domain and are therefore compared with the 27 km outer domain that produces the national

screening fields. Yanji (42.9° N, 129.5° E, ID 54292) is the regular radiosonde station closest to the case-study site and lies in the same region as the candidate sites identified in Northeast China, so that it provides the most direct test of the simulation at the site of interest; Nagqu (31.48° N, 92.07° E, ID 55299, 4508 m) and Xilinhot (43.95° N, 116.12° E, ID 54102, 1013 m) serve as reference stations in contrasting settings, representing a high-altitude continental plateau climate and a mid-latitude semi-arid grassland climate. At each station the hourly model output was paired with the sounding ascents available in 2024, and the paired profiles were interpolated to the same target height; identical statistics were computed for the three stations and the three variables, so that the results are directly comparable.

Air temperature is reproduced most accurately at all three stations (R = 0.979–0.996, RMSE = 1.13–2.37 °C), with regression slopes close to unity (0.96–1.07); relative humidity shows intermediate skill (R = 0.852–0.876, RMSE = 11.23–14.38%) and a consistent dry bias of 2.3–3.6%, largest at the driest of the three stations. Wind speed varies most among the stations (R = 0.758–0.908, RMSE = 2.07–3.49 m s^{-1}), but is essentially free of systematic bias at all of them: the NMB remains within 0.7%, including at Yanji, the station representative of the candidate region (−0.04 m s^{-1}, NMB = −0.4%). The regression slopes for wind speed nevertheless fall below unity everywhere (0.78–0.91), which indicates a slight underestimation of the high-wind tail rather than an error in the mean. The larger scatter at Nagqu is consistent with its position about 11 km from the nearest 27 km grid point, where the cell contains both the Nagqu River valley and the surrounding ranges, so that part of the residual error is representativeness error of the station rather than model error. Overall, the model reproduces the vertical structure of the three variables to a comparable standard in three contrasting regions of China, which indicates that the skill obtained at the candidate site is not specific to that site; the comparison nevertheless rests on a limited number of stations and on a single year of simulation.

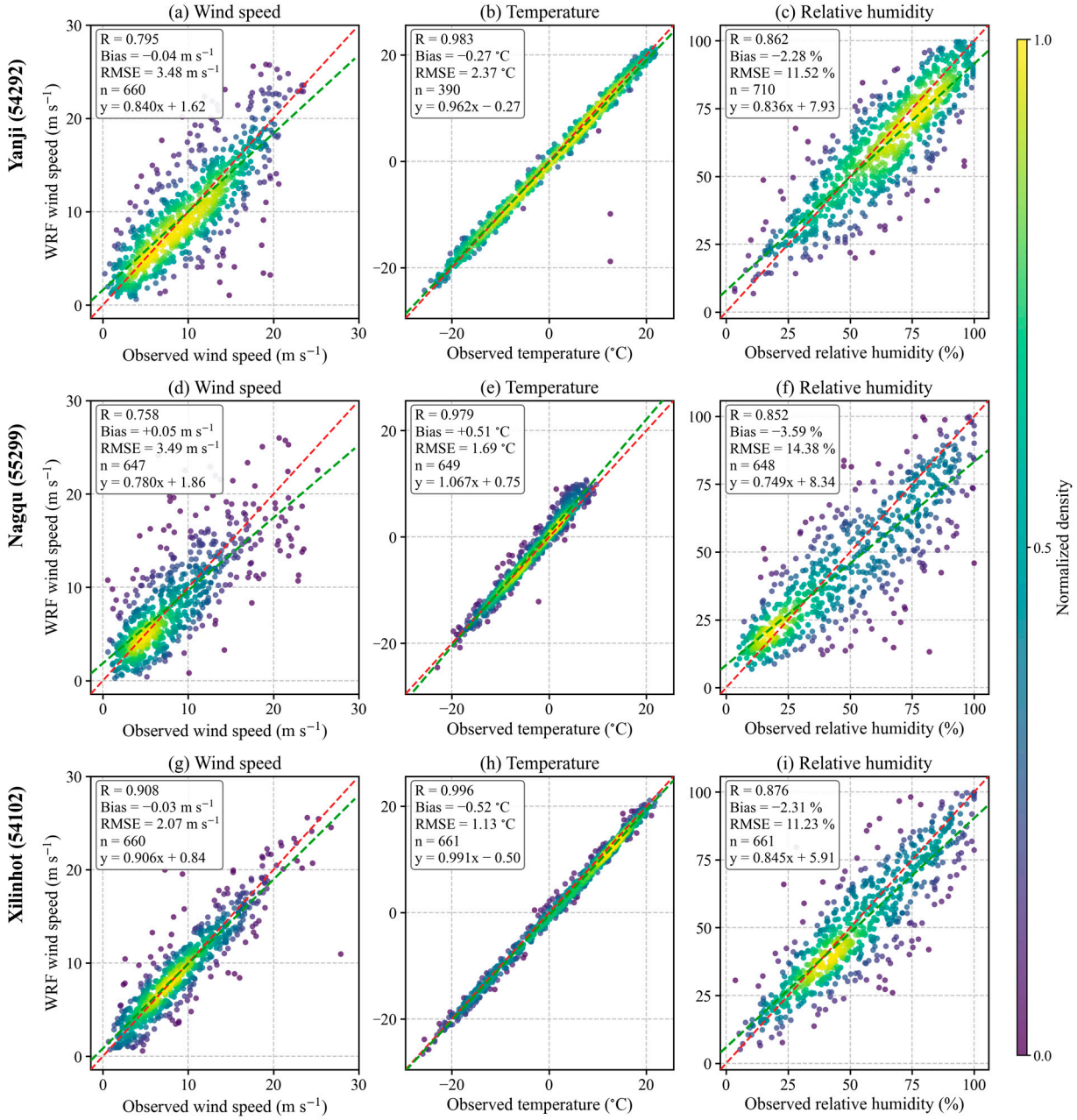


Figure 10. Comparison between WRF-simulated and radiosonde-observed profiles of (**a**,**d**,**g**) wind speed, (**b**,**e**,**h**) temperature and (**c**,**f**,**i**) relative humidity at (**a**–**c**) Yanji (54292) in Northeast China, the region of the candidate deployment sites, (**d**–**f**) Nagqu (55299) on the Tibetan Plateau and (**g**–**i**) Xilinhot (54102) on the Inner Mongolian Plateau. The red dashed line denotes the 1:1 reference line, and the green dashed line denotes the linear regression fit.

Table 3. Validation statistics of the WRF-simulated profiles against radiosonde observations at the three stations in 2024 (at 1000 m above ground level). The first block is the station representative of the candidate deployment region; the other two blocks are reference stations in contrasting regions.

Station	Variable	R	RMSE	NMB (%)
Yanji (54292)	Wind speed (m s^{-1})	0.795	3.48	−0.4
	Temperature (°C)	0.983	2.37	−10.2
	Relative humidity (%)	0.862	11.52	−3.7
Nagqu (55299)	Wind speed (m s^{-1})	0.758	3.49	+0.6
	Temperature (°C)	0.979	1.69	−16
	Relative humidity (%)	0.852	14.38	−7.5
Xilinhot (54102)	Wind speed (m s^{-1})	0.908	2.07	−0.3
	Temperature (°C)	0.996	1.13	−9
	Relative humidity (%)	0.876	11.23	−4.4

Wind rose analysis (Figure 11, left-hand panels) indicated that the prevailing wind direction at the candidate site was southwest, with seasonal variations in wind speed distribution. During winter (December to February), westerly winds dominate (frequency 28.4%), with wind speeds concentrated between 18 m/s and 20 m/s. During spring (March to May), the southwesterly winds intensified, with both southwesterly and westerly winds exceeding 20% frequency, and wind speeds primarily distributed between 8 and 20 m/s. During summer (June to August), high-frequency wind speeds continue to shift toward southwest winds, with southwest-to-west winds becoming the dominant direction. The wind speeds were concentrated between 4 and 12 m/s. In autumn (September to November), the westerly component strengthened again. Southwest-to-west winds remained the dominant direction, with the proportion of medium-to-high wind speeds (12–24 m/s) increasing to 14%.

Regarding the wind energy density distribution (Figure 11, right-hand panels), the west to southwest wind direction exhibited an extremely high energy concentration throughout the year, particularly in winter. The seasonal mean wind energy density in this direction ranges between about 490 W/m^2 in summer and 1770 W/m^2 in winter, reaching 1000–5000 W/m^2 during specific periods. This phenomenon primarily stems from the intensification of the mid-latitude westerly jet stream, making winter the season with the highest annual wind energy output. Spring wind speeds and energy densities, although slightly lower than winter, still maintain a high level of about 1640 W/m^2, with a more dominant southwest wind direction, exhibiting stable energy output characteristics. Although wind energy density in summer and autumn decreases compared to winter and spring, the increased frequency and intensity of southerly and southeasterly winds in summer reflect the influence of monsoon circulation. This variation partially balances energy supply from different wind directions throughout the year, mitigating the adverse effects of seasonal fluctuations. From a wind power development perspective, the consistent dominance of southwesterly winds significantly simplifies turbine layout and orientation optimizations. The high wind energy levels in spring and autumn, combined with the relatively stable conditions in summer and autumn, collectively form a balanced annual power generation distribution pattern.

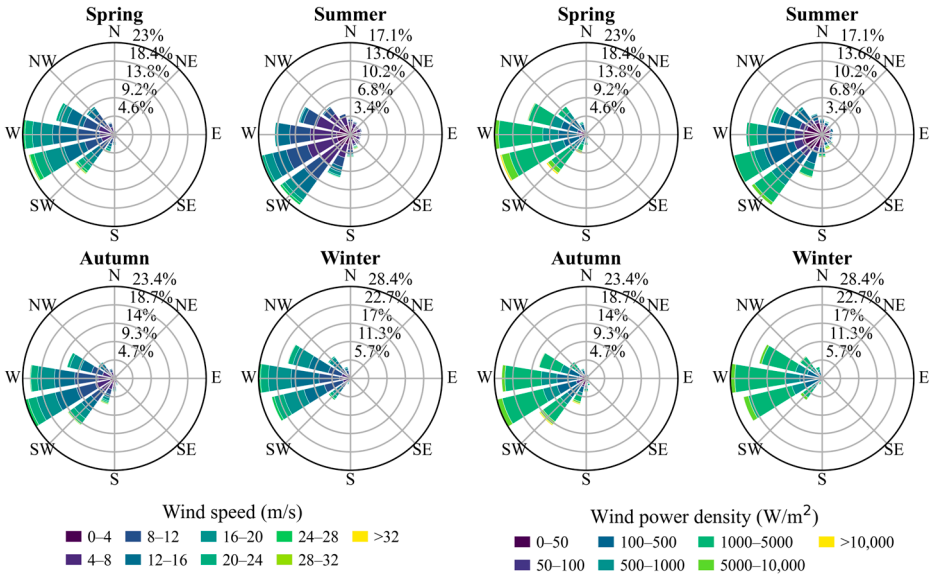


Figure 11. Seasonal wind rose diagrams for the candidate site: the left half of the figure shows wind speed and the right half wind power density, with the bin ranges given in the legends. Seasons are defined as spring (March–May), summer (June–August), autumn (September–November), and winter (December–February).

A more detailed analysis of the wind speed frequency distribution at the candidate site (Figure 12) indicated that spring winds predominantly ranged between 8 and 16 m/s, while winter winds shifted toward higher values, concentrating in the 12–16 m/s range. This reflects the wind energy enhancement effect of strong monsoons and cold air activity. Summer shows a shift towards the low-speed segment (2–6 m/s), while the transitional autumn season exhibits a bimodal distribution, revealing the seasonal variation patterns of wind energy resources and their climate-driven mechanisms.

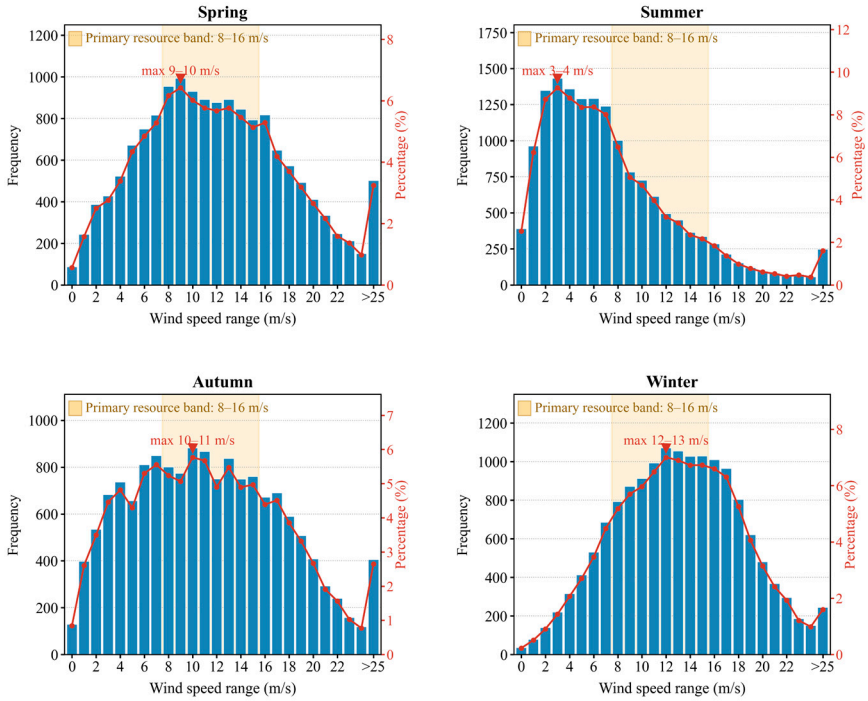


Figure 12. Seasonal wind speed frequency distribution at the candidate site (1 m/s bins). The shaded band marks the primary resource range of 8–16 m/s.

Comprehensively, the core annual wind speed range (about 54% of all hourly records) spans 6–16 m/s, encompassing the optimal operating wind speed (rated wind speed) of 15 m/s for wind turbines, indicating potential for equivalent full-load operating hours. A maximum of the frequency distribution occurs within the 6–8 m/s range, signifying strong persistence at medium wind speeds; the bin-by-bin distribution over the 8–16 m/s interval, which contains the bulk of the resource, is shown in Figure 12. From an operational risk perspective, events exceeding 30 m/s occur with less than 1% frequency, indicating minimal risk of wind turbine overload.

As shown in Figure 13, the candidate site exhibits a broad, smooth nocturnal maximum rather than a sharp peak: wind speeds and wind power densities both reach their highest values during the night and early morning period, with a broad maximum spanning 01:00–07:00 UTC+8 (Figure 13a: peak wind speed 11.91 m/s at 03:00; Figure 13b: peak wind power density 1492.90 W/m² at 07:00), whereas the afternoon period (12:00–16:00 UTC+8) at the site represents a low-value interval (wind speed 10.9 m/s, wind power density 1210 W/m²). Furthermore, at an altitude of 1000 m above ground level, the atmosphere approaches the geostrophic wind layer where turbulent friction effects are diminished, resulting in relatively minor diurnal variations.

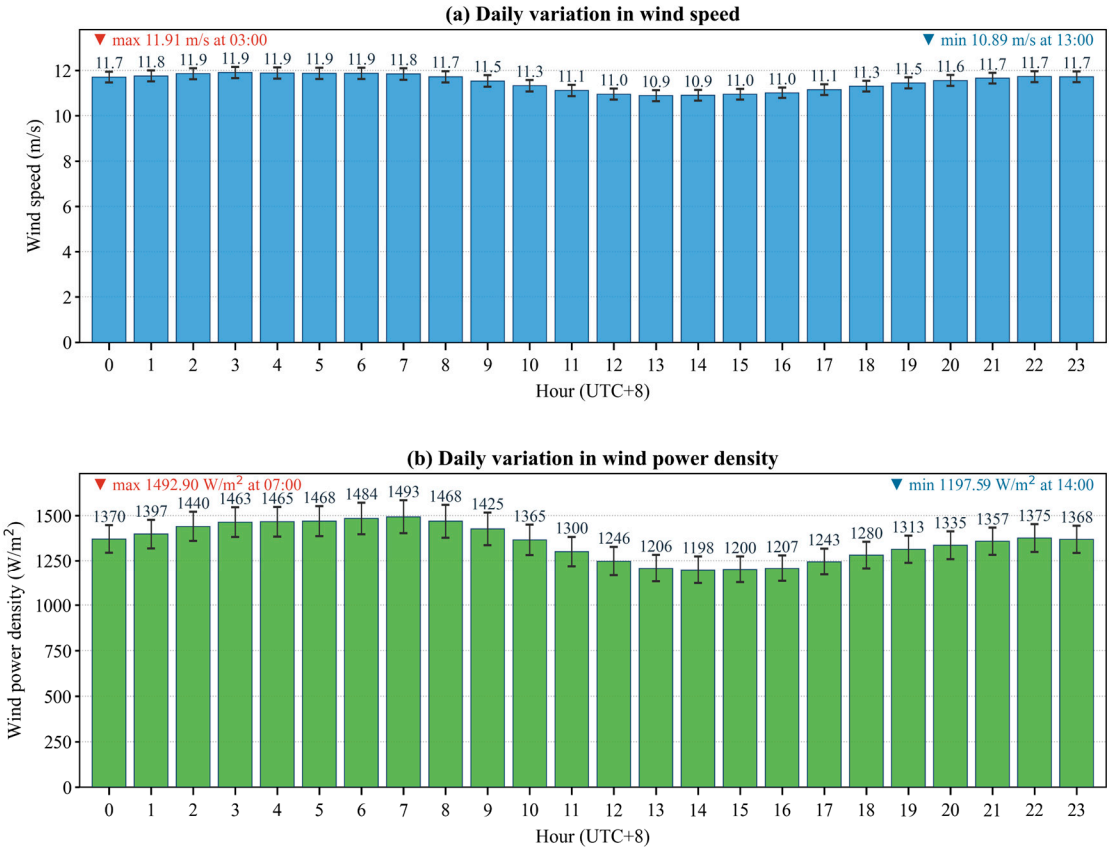


Figure 13. Daily variation at the candidate site: (**a**) wind speed; (**b**) wind power density.

As shown in Figure 14, the monthly variations in wind speed (Figure 14a) and wind power density (Figure 14b) at the candidate site indicate that both reach their annual maximum in December (mean wind speed 15.16 m/s, mean wind power density 2191 W/m²), forming a broad November–December maximum, since November is practically as energetic (14.75 m/s and 2191 W/m²); a further high-value period occurs in March (13.67 m/s and 1835 W/m²). Conversely, under the influence of the subtropical high-pressure system, both variables decline to their annual minimum in July (7.60 m/s and 556 W/m²), so that

July rather than August (7.83 m/s and 730 W/m²) is the least energetic month, wind power density then falling to about one quarter of its December value.

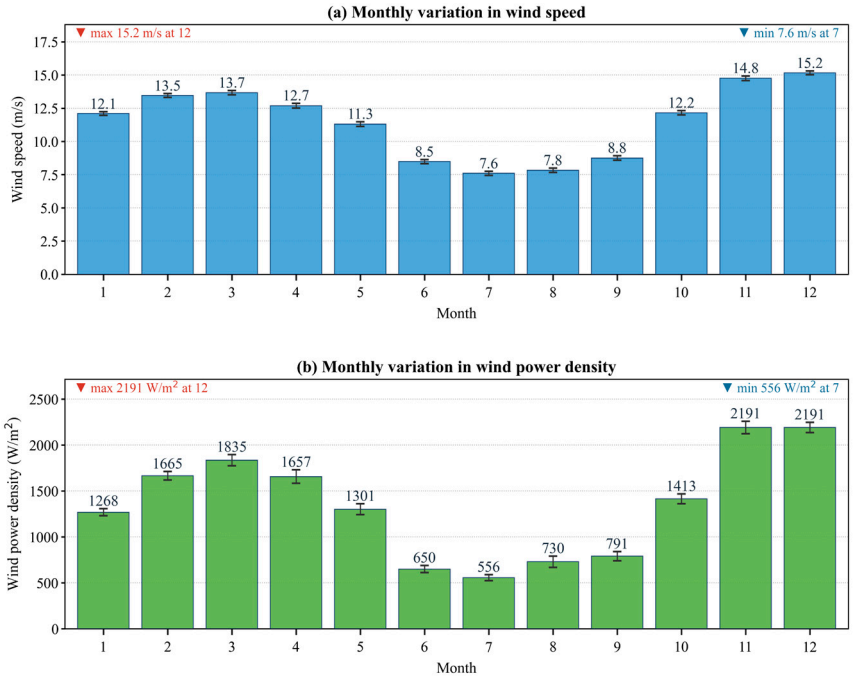


Figure 14. Monthly variation at the candidate site: (**a**) wind speed; (**b**) wind power density.

As summarized in Figure 15a, considering the seasonal variations in wind speed and power density, winter exhibits the most abundant wind energy resources, with an average wind speed of 13.58 m/s and a wind power density as high as 1709.29 W/m². Spring follows, featuring an average wind speed of 12.55 m/s and a wind power density of 1596.95 W/m². The seasonal mean wind speed and wind power density are 7.96 m/s and 645.46 W/m² in summer and 11.89 m/s and 1464.45 W/m² in autumn, so that summer is markedly weaker than autumn—by 3.9 m/s (+49%) in wind speed and 819 W/m² (+127%) in wind power density (Figure 15a,b). This asymmetry is consistent with the East Asian monsoon, in which summer subsidence and a reduced meridional temperature gradient suppress upper-level wind speeds over the study region. Consequently, tethered wind power systems require intelligent height-adjustment mechanisms to capture seasonal high-wind bands at varying altitudes, alongside optimized designs for extreme load resistance and tailored energy storage strategies.

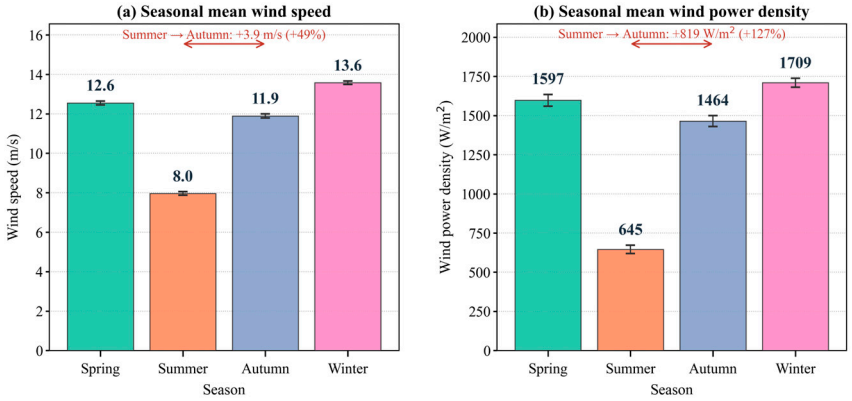


Figure 15. Seasonal variations at the candidate site: (**a**) mean wind speed; (**b**) mean wind power density. The red double-headed arrows denote the increase from summer to autumn, with the absolute and relative changes annotated.

4. Discussion

4.1. Analysis of Resource Distribution Characteristics

The spatial distribution of China's high-altitude wind energy resources is governed by the combined effects of atmospheric circulation systems, orographic dynamics and thermal effects. This results in pronounced regional and altitude-dependent patterns, with high wind power density zones concentrated in the Qinghai–Tibet Plateau, Yunnan-Guizhou Plateau, Inner Mongolia, Jilin, and other northeastern regions, as well as coastal areas. Within the altitude range considered here, both the mean wind speed and its short-term variability increase with height. This behaviour is not, however, unbounded: at higher levels, where the mean flow becomes very strong, short-term variability is reduced again. In this study, short-term variability is quantified by the standard deviation of the hourly wind speed within each season, seasonal variability by the winter-to-summer difference in the seasonal mean, and interannual variability by the coefficient of variation of the annual mean wind speed. This spatial pattern is consistent with the findings of Cai et al. [41] and He et al. [42]. Considering resource stability, engineering feasibility, and economic viability, this study focused on the 1000 m altitude layer.

From a spatial distribution perspective, the wind field is primarily governed by mid-to-high-latitude westerlies over Eurasia. Owing to the spatial positioning of the main axis of the westerly jet and its dynamic modulation by large-scale topography, the Tibetan Plateau, as a vast orographic barrier, compels the westerlies to flow around it and branch. Its northern margin lies on the right side of the jet stream's entrance zone, where wind speed convergence intensifies, forming a strong-wind belt. Central and eastern Inner Mongolia, situated at the eastern edge of the Mongolian Plateau, features open, flat terrain with low surface roughness. This topography is highly conducive to the transmission and maintenance of the westerly momentum. Consequently, the northern Tibetan Plateau and central-eastern Inner Mongolia constitute the core high wind speed zones. Moreover, the coastal regions of Northeast China, situated on the leeward side of the East Asian trough, serve as a crucial passage for temperate cyclones moving eastward into the sea, and similarly exhibit excellent wind energy resources. In contrast, the Sichuan and Tarim Basin, which are surrounded by high mountains, experience significant terrain-shielding effects. The lower atmosphere remains relatively stable, making it difficult for large-scale circulation to penetrate deeply, resulting in extensive areas of weak winds.

From a temporal perspective, the candidate sites exhibited a "stronger in winter, weaker in summer" pattern governed by the East Asian monsoon system. Ren et al. [23] found in their long-term observations that high-altitude winds in China show seasonal differences. At mid-to-high latitudes, winter pressure gradients yield abundant wind resources, while summer subsidence suppresses wind speeds. Notably, wind energy attenuation at 1000 m is substantially milder than at higher levels. This altitude generally lies above the atmospheric boundary layer in many regions, where turbulent mixing is significantly reduced. This ensures relatively consistent year-round availability and provides the physical basis for selecting 1000 m as the target development height. The resulting seasonal stability enhances capacity factors, improves economic predictability, and facilitates grid integration by easing seasonal balancing.

4.2. Uncertainty Analysis of Wind Energy Resource Assessment

In the case study of wind energy resource assessment at the candidate site described above, ERA5 reanalysis data were integrated with high-resolution WRF numerical simulations and a typical power curve of the generation system was coupled. Uncertainty nevertheless persists in the resulting estimate of generation potential, and two of its dominant sources are addressed here: the power curve assumed for the generating system, which governs the conversion of the wind resource into electricity, and the spatial representativeness of the ERA5 reanalysis, on which the nationwide screening rests. The processes that the present framework does not resolve are discussed at the end of this subsection.

The sensitivity of the generation-potential estimate to the assumed power curve was therefore quantified at the candidate site, where the standardized curve used throughout this study (cut-in 4 m/s, rated 15 m/s, cut-out 30 m/s) served as the reference. Because no measured power curve of an operational airborne wind energy system is available, the estimate was not anchored to a single design; instead, the parameters of the reference curve and two alternative curves representative of a more aggressive (3/12/25 m/s) and a more conservative (5/18/35 m/s) design were tested (Table 4). For this purpose the hourly wind speed statistics of the 25-year simulation were represented by a Weibull distribution fitted to the annual wind speed frequency distribution of the site (shape parameter k = 1.96, scale parameter c = 14.5 m/s) [43,44], which allows the generation integral to be evaluated analytically for each parameter set. The annual equivalent full-load operating hours were then recomputed with the cut-in, rated and cut-out speeds varied one at a time about the reference values (4, 15 and 30 m/s), with the theoretical capacity factor derived from these hours as defined in Section 2.5.2. The cut-in and cut-out speeds were found to exert only a modest influence on the outcome (at most about −4 to +1 percentage points in the theoretical capacity factor), whereas the rated wind speed is the dominant parameter, a change of ±3 m/s altering the capacity factor by about −11 to +12 percentage points. Across all tested parameter sets the capacity factor of the candidate site remains high (41.6–64.3%). More importantly, because the same standardized curve was applied to every grid cell nationwide, the relative ranking of sites and the spatial pattern of the screening are invariant to the choice of curve, and only the absolute scaling of the reported generation hours changes. The reported generation hours should accordingly be read as idealized, resource-based estimates whose absolute magnitude depends on the assumed curve, whereas the siting priorities derived from the resource ranking are insensitive to this choice.

Table 4. Sensitivity of the annual equivalent full-load operating hours and the capacity factor at the candidate site to the assumed power-curve parameters, computed from a Weibull fit (k = 1.96, c = 14.5 m/s) to the 2000–2024 hourly wind speed statistics.

Power-Curve Parameters (Cut-In/Rated/Cut-Out, m/s)	Annual Equivalent Full-Load Operating Hours (h)	Capacity Factor (%)	Change in Capacity Factor (Percentage Points)
Reference (4/15/30)	4566	52.1	—
Cut-in 3 m/s (3/15/30)	4604	52.6	+0.4
Cut-in 5 m/s (5/15/30)	4505	51.4	−0.7
Rated 12 m/s (4/12/30)	5630	64.3	+12.1
Rated 18 m/s (4/18/30)	3582	40.9	−11.2
Cut-out 25 m/s (4/15/25)	4225	48.2	−3.9
Cut-out 35 m/s (4/15/35)	4671	53.3	+1.2
Alternative curve A (3/12/25)	5342	61.0	+8.9
Alternative curve B (5/18/35)	3642	41.6	−10.5

A second source of uncertainty concerns the spatial representativeness of the input data. The 0.25° × 0.25° resolution of ERA5 smooths sub-grid orographic variability, and the representativeness error is largest in mountainous terrain, where the wind speed can differ substantially between adjacent slopes and across valley and gorge systems. Dynamical downscaling with WRF to 1 km substantially reduces, but does not eliminate, this limitation. The national maps derived from the reanalysis should therefore be read as a regional-scale characterization of the resource, and the site-specific values as an estimate that requires verification by in situ measurement before engineering design. Further dynamical downscaling and dedicated observational campaigns are the appropriate means of reducing the residual uncertainty. The two datasets are used at different scales and for different purposes and are therefore not expected to agree point by point. ERA5 provides a homogeneous, multi-decadal basis for macro-scale screening and for the ranking of broad regions, whereas the 1 km WRF simulation resolves the mesoscale flow that the reanalysis smooths and is used to refine and rank individual grid cells. The comparison presented in Section 3.3 is accordingly a consistency check between the simulation and the sounding observations at three stations in contrasting regions rather than a test of the equivalence of the two datasets. Two-tier strategies of this kind, in which a global reanalysis is used for screening and a limited-area model for refinement, are widely adopted in national and regional wind resource assessments [45–47].

Beyond these two quantified sources of uncertainty, several processes that shape the actual power output were not resolved by the present framework: the dynamic response of the airborne platform, tether and generator losses, and control-strategy efficiency, the reduction in air density with height, which was not applied to the rated wind speed, the influence of turbulence intensity on fatigue loads, and the variation of system efficiency with height and temperature [48,49]. Future studies should therefore couple aerodynamic, structural, and control models with simulations of specific turbine designs, so that the engineering credibility of power output predictions can be improved. The 1 km grid resolution of the candidate-site analysis is a further spatial limitation and calls for additional downscaling, which would make it possible to select typical sub-regions with abundant wind resources and relatively favorable development conditions. Multi-level nesting within a WRF-LES framework would enable simulations at much higher spatiotemporal resolution and provide an in-depth analysis of regional wind frequency distributions and wind direction stability [50–55]. This would allow the spatial proportion of high-efficiency wind zones and the total resource potential to be assessed, and would validate the effectiveness of high-resolution modeling for site selection under stringent constraints, thereby delivering high-confidence targeting for upper-level wind energy development.

At the practical engineering application level, beyond wind resource conditions, potential sub-regions must be selected by systematically integrating multidimensional constraints [56]. Key considerations include engineering and economic factors, such as terrain complexity, infrastructure availability, and construction difficulty. The multi-height results presented in Section 3.1 show that wind speed and wind power density continue to increase with height (Figures 3 and 4), indicating further development potential at 2000 m and above; development at these altitudes nevertheless faces more demanding requirements on system reliability and higher costs. Subsequent research should therefore focus on identifying the optimal development height and on systematic techno-economic evaluation, so that high-altitude wind energy can move from resource potential to substantive economic viability.

4.3. Technical Feasibility and Economic Outlook

At 1000 m altitude, the Qinghai–Tibet Plateau, central-eastern Inner Mongolia, and eastern coastal regions of Northeast China demonstrate immense potential, where annual

equivalent full-load operating hours exceed 3000 h over large areas and surpass 4000 h in the most favourable zones, corresponding to a theoretical capacity factor above 45%. Tethered airborne power generation systems are currently regarded as the most promising engineering pathway owing to their technical advantages, including high platform stability and strong load-bearing capacity [57]. However, converting this potential into a stable and reliable power output requires overcoming a series of technical and engineering hurdles. The materials and structures of the system must withstand intense wind loads, extreme temperature fluctuations, potent ultraviolet radiation, and potential threats from icing and lightning strikes at high altitudes. This necessitates the development of next-generation high-performance composites, durable tether cables, and lightweight yet robust generator pod designs [58,59]. Intelligent control strategies are pivotal for maximizing safety and efficiency. These systems must dynamically adjust flight attitude and altitude in real time to precisely track optimal wind zones while autonomously executing avoidance or safe recovery protocols during extreme conditions [16].

Looking ahead, by prioritizing demonstration projects in regions with favorable high-altitude wind resources, such as the Qinghai–Tibet Plateau, Inner Mongolia, and the northeastern coastal areas identified in this study, we can accumulate operational data and iterate technologies.

5. Conclusions

A nationwide systematic assessment of upper-level wind energy resources in China was performed, with emphasis on a target altitude of 1000 m. By integrating ERA5 reanalysis, WRF mesoscale simulations, and a generation potential model driven by typical power curves, a multi-scale technical framework spanning macro-distribution to site-specific refinement was established.

The northern Qinghai–Tibet Plateau and central-eastern Inner Mongolia were identified as core resource-rich zones, resulting from the combined effect of the westerly jet and orographic lifting. Eastern coastal areas of Jilin Province, influenced by mid-latitude cyclone tracks, also exhibited stable, high-quality wind resources at 1000 m. Temporal analysis further demonstrated that the 1000 m level captures winter wind energy maxima while substantially mitigating the severe interannual and seasonal fluctuations observed at higher altitudes, thus providing a favorable trade-off between resource stability and technical feasibility at this selected reference level. Coupling meteorological fields with power curves yielded annual equivalent full-load hours consistently exceeding 4000 h in the Qinghai–Tibet Plateau, Inner Mongolia Plateau, and northeastern coastal zones, corresponding to a theoretical capacity factor above 45%. This highlights the potential of high-altitude wind to contribute as a baseload resource in high-penetration renewable systems. The proposed multi-scale siting procedure identified and prioritized multiple development sites across Inner Mongolia, Qinghai, Tibet, and Northeast China, directly supporting demonstration project planning.

A detailed case study in coastal Jilin Province validated the framework. WRF simulations reproduced the observed wind speed, temperature and relative humidity with correlation coefficients above 0.75, 0.97 and 0.85 at 1000 m above ground level at three stations in contrasting regions, revealing a prevailing southwesterly–westerly wind regime, high energy concentration, and low frequency of extreme winds. Diurnal and seasonal patterns were quantified: wind speeds were lower during daytime and higher at night, and greater in winter than in summer. These site-specific characteristics provide a quantitative basis for micro-siting, turbine layout, structural load calculations, and operational strategy design.

This work addresses a critical gap in China's high-altitude wind resource assessment and delivers scientific evidence, methodological tools, and foundational data to advance

the technology from concept to engineering deployment. Several limitations of the present framework should be acknowledged. First, the generation potential is derived from a single standardized power curve, so that the reported equivalent full-load hours are idealized, resource-based estimates rather than predictions for a specific device; a sensitivity test with alternative assumed parameters at the candidate site shows that the relative resource ranking is insensitive to this choice, although the absolute values rescale; coupling aerodynamic, structural and control models to the simulation of a particular airborne system is the necessary next step. Second, although the WRF output has now been evaluated against sounding observations at three stations in contrasting regions, namely Northeast China, the Qinghai–Tibet Plateau and Inner Mongolia, and the model reproduces the observed wind speed, air temperature and relative humidity to a comparable standard at all three, these comparisons rest on a single year of data and on point measurements at 1000 m above ground level, so that a denser network of stations together with dedicated observational campaigns is still required before the national conclusions can be regarded as fully established. Third, the 1 km resolution of the nested simulation cannot resolve microtopographic features such as gullies and ridges, so that further downscaling is needed for engineering design at a specific site. Fourth, the altitude of 1000 m is treated as a selected reference level rather than as a demonstrated optimum, and a systematic techno-economic optimization of the deployment altitude remains to be carried out. Finally, airspace management, safety regulation and the certification of tethered systems are not addressed here, although they will condition the pace of commercial deployment.

Future commercialization will depend on continued progress in low-cost, high-performance materials, intelligent disturbance-resilient control, airspace coordination, and life-cycle cost optimization. With sustained technological maturation and policy support, high-altitude wind energy can become a strategic pillar in China's transition to a clean, low-carbon and efficient energy system.

Author Contributions: Conceptualization, X.S., H.X. and L.G.; methodology, X.S., H.X. and L.G.; software, Q.L., W.X. and M.W.; validation, Z.L. and M.W.; formal analysis, Q.L. and Z.L.; investigation, Q.L., Z.L., Z.C. and M.W.; resources, W.X., M.W., C.Z. and H.Z.; data curation, W.X. and M.W.; writing—original draft preparation, Q.L. and Z.L.; writing—review and editing, X.S., H.X. and L.G.; visualization, W.X. and Z.L.; supervision, X.S. and Q.L.; project administration, X.S.; funding acquisition, X.S. All authors have read and agreed to the published version of the manuscript.

Funding: This research was funded by a research project of Power China Guiyang Engineering Corporation Limited (Research on Key Technologies for Planning, Design and Construction of Airborne Wind Energy, grant number YJZDXM240014).

Data Availability Statement: The ERA5 reanalysis data can be found at the Copernicus Climate Data Store (https://cds.climate.copernicus.eu/) (accessed on 20 July 2025). The sounding observation data can be found at the University of Wyoming upper-air archive (https://weather.uwyo.edu/upperair/sounding.shtml) (accessed on 20 July 2025).

Acknowledgments: We acknowledge all the anonymous reviewers for their comments, which helped to improve the original manuscript.

Conflicts of Interest: Xiong Song, Huawei Xiang and Lanqiang Gong were employed by the Power China Guiyang Engineering Corporation Limited. Wenyue Xue, Zijun Luo, Menglong Wang, Chunling Zhou, Hong Zhang, Zhe Cai and Qiang Liu were employed by the Nanjing Climblue Technology Co. The paper reflects the views of the scientists and not the company.

Abbreviations

AGL above ground level; AWE airborne wind energy; CF capacity factor; ECMWF European Centre for Medium-Range Weather Forecasts; ERA5 ECMWF Reanalysis v5; LSM land surface model; NMB normalized mean bias; PBL planetary boundary layer; R correlation coefficient; RMSE root mean square error; RRTM Rapid Radiative Transfer Model; WRF Weather Research and Forecasting; YSU Yonsei University.

Nomenclature

Symbols: α wind shear exponent; ϱ air density (kg/m^3); g gravitational acceleration (m/s^2); T air temperature (K); u wind speed (m/s); U, V, W zonal, meridional and vertical wind components (m/s); Z geopotential (m^2/s^2); Zs surface geopotential (m^2/s^2); P wind power density (W/m^2); pd dry air partial pressure (Pa); e water vapour pressure (Pa); es saturation water vapour pressure (Pa); Rd gas constant of dry air (287.058 J/(kg·K)); Rv gas constant of water vapour (461.5 J/(kg·K)); rh relative humidity; N number of samples; Heq annual equivalent full-load operating hours (h); CF capacity factor.

References

1. IPCC. *Climate Change 2022: Impacts, Adaptation and Vulnerability. Contribution of Working Group II to the Sixth Assessment Report of the Intergovernmental Panel on Climate Change*; Cambridge University Press: Cambridge, UK, 2022.
2. International Energy Agency (IEA). *World Energy Outlook 2023*; IEA: Paris, France, 2023.
3. Tsinghua University Carbon Neutrality Research Institute. *Technology Outlook on Wind and Solar Power Toward China's Carbon Neutrality Goal*; Tsinghua University: Beijing, China, 2024. (In Chinese)
4. GWEC (Global Wind Energy Council). *Global Wind Report 2026*; GWEC: Brussels, Belgium, 2026.
5. Global Wind Energy Council (GWEC). *Global Wind Report 2024*; GWEC: Brussels, Belgium, 2024. Available online: https://gwec.net/gwec-releases-global-wind-report-2024/ (accessed on 16 April 2024).
6. IEA. *Energy Technology Perspectives 2024*; IEA: Paris, France, 2024.
7. Chinese Renewable Energy Association, Wind Energy Professional Committee (CWEA). 2024 China wind power installation capacity statistical brief. *Wind Energy* **2025**, 3, 48–63. (In Chinese)
8. Zhuo, Z.Y.; Zhang, N.; Xie, X.R.; Li, H.Z.; Kang, C.Q. Key technologies and developing challenges of power system with high proportion of renewable energy. *Autom. Electr. Power Syst.* **2021**, *45*, 171–191. https://doi.org/10.7500/AEPS20200922001. Available online: https://max.book118.com/html/2023/0919/7131145106005160.shtm (accessed on 15 October 2026). (In Chinese)
9. Archer, C.L.; Caldeira, K. Global assessment of high-altitude wind power. *Energies* **2009**, *2*, 307–319. https://doi.org/10.3390/en20200307.
10. Loyd, M.L. Crosswind kite power. *J. Energy* **1980**, *4*, 106–111. https://doi.org/10.2514/3.48021.
11. Marvel, K.; Kravitz, B.; Caldeira, K. Geophysical limits to global wind power. *Nat. Clim. Change* **2013**, *3*, 118–121. https://doi.org/10.1038/nclimate1683.
12. Ahrens, U.; Diehl, M.; Schmehl, R. (Eds.) *Airborne Wind Energy*; Springer: Berlin/Heidelberg, Germany, 2013.
13. Fagiano, L.; Milanese, M. Airborne wind energy: An overview. In Proceedings of the 2012 American Control Conference, Montreal, QC, Canada, 27–29 June 2012; IEEE: Piscataway, NJ, USA, 2012; pp. 3132–3143. https://doi.org/10.1109/acc.2012.6314801.
14. Cherubini, A.; Papini, A.; Vertechy, R.; Fontana, M. Airborne wind energy systems: A review of the technologies. *Renew. Sustain. Energy Rev.* **2015**, *51*, 1461–1476. https://doi.org/10.1016/j.rser.2015.07.053.
15. Roberts, B.W.; Shepard, D.H.; Caldeira, K.; Cannon, M.E.; Eccles, D.G.; Grenier, A.J.; Freidin, J.F. Harnessing high-altitude wind power. *IEEE Trans. Energy Convers.* **2007**, *22*, 136–144. https://doi.org/10.1109/TEC.2006.889603.
16. Canale, M.; Fagiano, L.; Milanese, M. High altitude wind energy generation using controlled power kites. *IEEE Trans. Control Syst. Technol.* **2010**, *18*, 279–293. https://doi.org/10.1109/TCST.2009.2017933.
17. Shao, L.; Mao, H.; Xing, S.; Li, W.; Fang, Z.; Hou, Y. A review of the development status and key technologies of high-altitude wind power generation. *Adv. New Energy* **2020**, *8*, 477–485. https://doi.org/10.3969/j.issn.2095-560X.2020.06.005. (In Chinese)
18. Jiang, Y.; Lu, C.; Yuan, Z.; Guo, P.; Liu, D. Energy Capture and Conversion Technology of High Altitude Wind Power Generation Systems: Current Situation and Prospect. *Proc. CSEE* **2025**, *45*, 8365–8377. https://doi.org/10.13334/j.0258-8013.pcsee.241569. (In Chinese)

19. Ma, G.L.; Li, J.; Song, Y.; Tian, L.; Liu, X.; Zhao, N. A Study on Wind Resource Assessment for Complex Mountain Wind Farms Based on Coupled Mesoscale-Microscale Technology. *Energy Power J.* **2025**, 642 – 654. https://doi.org/10.19912/j.0254-0096.tynxb.2024-1001. (In Chinese)
20. Han, S.; Li, J.; Zhao, Y. Key Technologies, Current Status, and Development Trends of High-Altitude Wind Power. *Distributed Energy* **2024**, *9*, 1–9. https://doi.org/10.16513/j.2096-2185.DE.2409101. (In Chinese)
21. Sohoni, V.; Gupta, S.C.; Nema, R.K. A Critical Review on Wind Turbine Power Curve Modelling Techniques and Their Applications in Wind Based Energy Systems. *J. Energy* **2016**, 8519785. https://doi.org/10.1155/2016/8519785.
22. Hersbach, H.; Bell, B.; Berrisford, P.; Hirahara, S.; Horányi, A.; Muñoz-Sabater, J.; Nicolas, J.; Peubey, C.; Radu, R.; Schepers, D.; et al. The ERA5 global reanalysis. *Q. J. R. Meteorol. Soc.* **2020**, *146*, 1999–2049. https://doi.org/10.1002/qj.3803.
23. Ren, G.Y.; Zhang, A.Y.; Wang, Y.; Guo, J. Climatology of upper wind speeds over China. *Geogr. Res.* **2009**, *28*, 1583–1592. https://doi.org/10.11821/yj2009060014. (In Chinese)
24. Mangsuer, A.; Xiao, J.; Sun, M.; Tang, H. Comparative analysis on the applicability of ERA5 and FNL data in Xinjiang. *Plateau Mt. Meteorol. Res.* **2024**, *44*, 142–150. https://doi.org/10.3969/j.issn.1674-2184.2024.04.016. (In Chinese)
25. Liang, S.C.; Zhang, X.D.; Kang, S.; Kang, S.; Kang, Y.L.; Zhao, Y.F. Wind resource assessment method over complex terrain based on numerical simulation. *Acta Aerodyn. Sin.* **2012**, *30*, 415–420. (In Chinese)
26. Lin, Y.-L.; Farley, R.D.; Orville, H.D. Bulk parameterization of the snow field in a cloud model. *J. Clim. Appl. Meteorol.* **1983**, *22*, 1065–1092. https://doi.org/10.1175/1520-0450(1983)022<1065:BPOTSF>2.0.CO;2.
27. Kain, J.S.; Fritsch, J.M. A one-dimensional entraining/detraining plume model and its application in convective parameterization. *J. Atmos. Sci.* **1990**, *47*, 2784–2802.
28. Kain, J.S.; Fritsch, J.M. Convective parameterization for mesoscale models: The Kain–Fritsch scheme. In *The Representation of Cumulus Convection in Numerical Models*; Meteor. Monogr., No. 46; Emanuel, K.A., Raymond, D.J., Eds.; American Meteorological Society: Boston, MA, USA, 1993; pp. 165–170.
29. Kain, J.S. The Kain–Fritsch convective parameterization: An update. *J. Appl. Meteorol*. **2004**, *43*, 170–181. https://doi.org/10.1175/1520-0450(2004)043<0170:TKCPAU>2.0.CO;2.
30. Mlawer, E.J.; Taubman, S.J.; Brown, P.D.; Iacono, M.J.; Clough, S.A. Radiative transfer for inhomogeneous atmospheres: RRTM, a validated correlated-k model for the longwave. *J. Geophys. Res. Atmos*. **1997**, *102*, 16663–16682. https://doi.org/10.1029/97JD00237.
31. Chou, M.-D.; Suarez, M.J. *A Solar Radiation Parameterization for Atmospheric Studies*; NASA Tech. Memo. 104606; NASA Goddard Space Flight Center: Greenbelt, MD, USA, 1999; Volume 15.
32. Monin, A.S.; Obukhov, A.M. Basic laws of turbulent mixing in the ground layer of the atmosphere. *Contrib. Geophys. Inst. Acad. Sci. USSR* **1954**, *151*, 163–187.
33. Chen, F.; Dudhia, J. Coupling an advanced land surface–hydrology model with the Penn State–NCAR MM5 modeling system. Part I: Model implementation and sensitivity. *Mon. Weather Rev.* **2001**, *129*, 569–585. https://doi.org/10.1175/1520-0493(2001)129<0569:CAALSH>2.0.CO;2.
34. Hong, S.-Y.; Noh, Y.; Dudhia, J. A new vertical diffusion package with an explicit treatment of entrainment processes. *Mon. Weather Rev.* **2006**, *134*, 2318–2341. https://doi.org/10.1175/MWR3199.1.
35. Hodson, T.O. Root mean square error (RMSE) or mean absolute error (MAE): When to use them or not. *Geosci. Model Dev.* **2022**, *15*, 5481–5487. https://doi.org/10.5194/gmd-15-5481-2022.
36. Ning, H. Enhancing public health surveillance: SARIMAX model incorporating Baidu search index for HCV prediction in China. *BMC Med. Res. Methodol.* **2025**, *25*, 108. https://doi.org/10.1186/s12874-025-02562-w.
37. Dobesch, H.; Kury, G. *Basic Meteorological Concepts and Recommendations for the Exploitation of Wind Energy in the Atmospheric Boundary Layer*; Zentralanstalt für Meteorologie und Geodynamik: Wien, Austria, 2006; pp. 103–105.
38. Bolton, D. The computation of equivalent potential temperature. *Mon. Weather Rev.* **1980**, *108*, 1046–1053. https://doi.org/10.1175/1520-0493(1980)108<1046:TCOEPT>2.0.CO;2.
39. Buck, A.L. New equations for computing vapor pressure and enhancement factor. *J. Appl. Meteorol.* **1981**, *20*, 1527–1532. https://doi.org/10.1175/1520-0450(1981)020<1527:NEFCVP>2.0.CO;2.
40. Compilation Group of Inner Mongolia Wind Energy Resource Assessment. *Inner Mongolia Wind Energy Resource Assessment*; Meteorological Press: Beijing, China, 2022. (In Chinese)
41. Cai, Y.F.; Li, X.Y.; Ren, Z.D.; Sun, S. Wind energy resource analysis for airborne wind power generation systems. *Acta Energ. Sol. Sin.* **2025**, *46*, 624–632. https://doi.org/10.19912/j.0254-0096.tynxb.2023-1635. (In Chinese)

42. He, H.; Niu, X.J. Distribution characteristics of high-altitude wind resources in China. *J. Hydroelectr. Eng.* **2025**, *44*, 28–37. https://doi.org/10.11660/slfdxb.20250203. (In Chinese)
43. Justus, C.G.; Hargraves, W.R.; Yalcin, A. Nationwide assessment of potential output from wind-powered generators. *J. Appl. Meteorol*. **1976**, *15*, 673–678. https://doi.org/10.1175/1520-0450(1976)015<0673:NAOPOF>2.0.CO;2.
44. Carta, J.A.; Ramírez, P.; Velázquez, S. A review of wind speed probability distributions used in wind energy analysis: Case studies in the Canary Islands. Renew. *Sustain. Energy Rev*. **2009**, *13*, 933–955. https://doi.org/10.1016/j.rser.2008.05.005.
45. Olauson, J. ERA5: The new champion of wind power modelling? *Renew. Energy* **2018**, *126*, 322–331. https://doi.org/10.1016/j.renene.2018.03.056.
46. Coimbra, I.L.; Palma, J.M.L.M. Synoptic and mesoscale winds in the complex terrain of Perdigão. *J. Phys. Conf. Ser*. **2022**, *2265*, 022010. https://doi.org/10.1088/1742-6596/2265/2/022010.
47. Jiménez-Garrote, A.; Santos-Alamillos, F.J.; Sánchez-Hernández, G.; López-Cuesta, M.; Ruiz-Arias, J.A.; Pozo-Vázquez, D. Evaluation of a database of the Spanish wind energy resources derived from a regional reanalysis. *Energies* **2024**, *17*, 1523. https://doi.org/10.3390/en17071523.
48. Ali, Q.S.; Kim, M.H. Power conversion performance of airborne wind turbine under unsteady loads. *Renew. Sustain. Energy Rev*. **2022**, *153*, 111798. https://doi.org/10.1016/j.rser.2021.111798.
49. Frirdich, A. Rotor Design Procedure for a Drag Power Kite. Ph.D. Thesis, Technischen Universität München, Munich, Germany, 2019.
50. Arya, S.P.S.; Capuano, M.E.; Fagen, L.C. Some fluid modeling studies of flow and dispersion over two-dimensional low hills. *Atmos. Environ.* **1987**, *21*, 753–764. https://doi.org/10.1016/0004-6981(87)90071-0.
51. Kadivar, M.; Tormey, D.; McGranaghan, G. A review on turbulent flow over rough surfaces: Fundamentals and theories. *Int. J. Thermofluids* **2021**, *10*, 100077. https://doi.org/10.1016/j.ijft.2021.100077.
52. Batt, R.; Gant, S.; Lacome, J.M.; Truchot, B.; Tucker, H. CFD modelling of dispersion in neutrally and stably-stratified atmospheric boundary layers: Results for Prairie Grass and Thorney Island. *Int. J. Environ. Pollut.* **2018**, *63*, 1–18. https://doi.org/10.1504/IJEP.2018.093026.
53. Thordal, M.S.; Bennetsen, J.C.; Koss, H.H.H. Review for practical application of CFD for the determination of wind load on high-rise buildings. *J. Wind Eng. Ind. Aerodyn.* **2019**, *186*, 155–168. https://doi.org/10.1016/j.jweia.2018.12.019.
54. Hu, W.C.; Yang, Q.S.; Chen, H.P.; Yuan, Z.; Li, C.; Shao, S.; Zhang, J. Wind field characteristics over hilly and complex terrain in turbulent boundary layers. *Energy* **2021**, *224*, 120070. https://doi.org/10.1016/j.energy.2021.120070.
55. Liu, Y.J.; Miao, S.G.; Hu, F.; Liu, B.Y. Large eddy simulation of boundary layer wind field in Xiaohaituo Mountain area of Winter Olympics. *Plateau Meteorol*. **2018**, *37*, 1388–1401. http://www.gyqx.ac.cn/CN/10.7522/j.issn.1000-0534.2018.00034. (In Chinese)
56. Zhao, L.; Wei, C.; Wang, Y.; Qiu, Y.F.; Dong, F. Macro-siting and wind energy resource reserve estimation for offshore wind farms. *Acta Energ. Sol. Sin*. **2024**, *45*, 1–8. https://doi.org/10.19912/j.0254-0096.tynxb.2023-1378. (In Chinese)
57. Ran, X.L. Dynamics and Control of Traction Parafoil for High-Altitude Wind Energy Generation. Ph.D. Thesis, National University of Defense Technology, Changsha, China, 2012. (In Chinese)
58. Sieberling, S.; Ruiterkamp, R. The PowerPlane: An airborne wind energy system—Conceptual operations. In *Proceedings of the 11th AIAA Aviation Technology, Integration, and Operations (ATIO) Conference, Virginia Beach, VA, USA, 20–22 September 2011*; AIAA: Reston, VA, USA, 2011. https://doi.org/10.2514/6.2011-6909.
59. Joshi, R.; von Terzi, D.; Schmehl, R. System design and scaling trends in airborne wind energy demonstrated for a ground-generation concept. *Wind Energy Sci.* **2025**, *10*, 695–716. https://doi.org/10.5194/wes-10-695-2025.

Disclaimer/Publisher's Note: The statements, opinions and data contained in all publications are solely those of the individual author(s) and contributor(s) and not of MDPI and/or the editor(s). MDPI and/or the editor(s) disclaim responsibility for any injury to people or property resulting from any ideas, methods, instructions or products referred to in the content.